Materials Horizons

ROYAL SOCIETY OF CHEMISTRY

REVIEW

View Article Online
View Journal | View Issue

Cite this: *Mater. Horiz.*, 2023, 10, 4686

Origin and characterization of the oxygen loss phenomenon in the layered oxide cathodes of Li-ion batteries†

Junrun Feng, Zhuo Chen, Weihua Zhou and Zhangxiang Hao *

Li-ion batteries have been widely applied in the field of energy storage due to their high energy density and environment friendliness. Owing to their high capacity of ~200 mA h g^{-1} and high cutoff voltage of ~4.6 V *vs.* Li^+/Li, layered lithium transition metal oxides (LLMOs) stand out among the numerous cathode materials. However, the oxygen loss of LLMO cathodes during cycling hampers the further development LLMO cathode-based Li-ion batteries by inducing a dramatic decay of electrochemical performance and safety issues. In this regard, the oxygen loss phenomenon of LLMO cathodes has attracted attention, and extensive efforts have been devoted to investigating the origins of oxygen loss in LLMO cathodes by various characterization methods. In this review, a comprehensive overview of the main causes of oxygen loss is presented, including the state of charge, side reactions with electrolytes, and the thermal instability of LLMO cathodes. The characterization methods used in the scope are introduced and summarized based on their functional principles. It is hoped that the review can inspire a deeper consideration of the utilization of characterization techniques in detecting the oxygen loss of LLMO cathodes, paving a new pathway for developing advanced LLMO cathodes with better cycling stability and practical capabilities.

Received 23rd May 2023,
Accepted 2nd August 2023

DOI: 10.1039/d3mh00780d

rsc.li/materials-horizons

Wider impact

Layered lithium transition metal oxide (LLMO) cathodes with a high capacity of ~200 mA h g^{-1} and a high cutoff voltage of ~4.6 V *vs.* Li^+/Li stand out among the numerous cathode materials of Li-ion batteries. However, current LLMO cathode-based Li-ion batteries still suffer from the electrochemical performance decay and safety concerns during long-term operation, which is contributed by the oxygen loss phenomenon of the LLMO cathode. The lack of understanding of the origins of oxygen loss and the functional principle of these methods is becoming the bottleneck of the field. In this regard, this review summarizes the current understanding of the origins of oxygen loss in LLMO cathodes, reviews recent efforts to develop advanced and suitable characterization techniques, and illustrates the capabilities and limitations of these methods. The review will inspire the development of next-generation characterization techniques and enhance the comprehensive understanding of oxygen loss in LLMO-based Li-ion batteries.

1. Introduction

Li-ion batteries have been widely used in electric vehicles, portable devices, and grid energy storage since the invention of rocking chair batteries by Sony Energytech Inc. in the 1990s.[1–4] Layered lithium transition metal oxide (LLMO) cathodes with the advantages of high practical capacity (~200 mA h g^{-1}) and high cutoff voltage (~4.6 V *vs.* Li^+/Li) are rising as a shining star among the numerous cathode materials.[5–8] LLMO cathodes are normally described with a formula of $LiMO_2$ (M stands for transition metals such as Ni, Co, Mn, Ti, and Al) and a layered crystallographic space group $R\bar{3}m$.[9–12] The typical layered structure allows the reversible shuttling of Li-ions in the structure.[13] Although various LLMO cathodes have been successfully applied in commercialized Li-ion batteries, they still suffer from limitations such as capacity decay, voltage drop, and coulombic efficiency reduction during the long-term operation.[14–16] Moreover, safety concerns resulting from the explosion and ignition of cells also limit the further application of LLMO cathode-based Li-ion batteries in large-scale energy storage systems.[17] With extensive research in the field, the issues are found to be contributed by the oxygen loss phenomenon of LLMO cathodes during cycling, which results in the structural degradation and chemical evolution of cathodes, electrolytes and even the whole cell.[18,19] More

School of Science, School of Chip Industry, Hubei University of Technology, Wuhan, Hubei 430068, China. E-mail: haozx@hbut.edu.cn

† Electronic supplementary information (ESI) available. See DOI: https://doi.org/10.1039/d3mh00780d

specifically, as the cathode structure is supported by an oxygen framework, the oxygen loss easily leads to phase transformations[20] and defect formation[21] in the structure, promoting degradation such as lattice amorphization and cathode cracking.[10,22–25] Furthermore, the released oxygen existing as O_2 or O^{2-} will participate in the interfacial reaction between cathodes and electrolytes, forming gaseous products (CO_2, CO, H_2O, *etc.*) and cathode-electrolyte interfaces (CEIs).[26–29] The interfaces and gaseous products formed will intensify the safety concerns of Li-ion batteries by triggering the thermal runaway phenomenon during cycling.[24,30] Thermal runaway is commonly observed in Li-ion batteries as a electrochemical process and unexpected interfacial reactions could rise the temperature of cells, which will further accelerate the side reaction and decomposition of cell components, decay the battery performance and possibly ignite the cell.[31,32] Therefore, the oxygen loss of the LLMO cathode is a critical issue in further optimizing the durability and safety of next-generation Li-ion battery systems.

In recent decades, numerous works have been conducted to inhibit the oxygen loss phenomenon of LLMO cathodes, which have been comprehensively summarized in other studies reported in the literature.[19,33–35] However, these methods such as surface coating[36,37] and composition modification[38] are still insufficient to suppress the oxygen evolution.[10,18,35] The lack of understanding of the origins of oxygen loss and the functional principle of these methods is becoming the bottleneck of the field.[18,35] Advanced characterization methods are required to provide deeper insights, especially under practical conditions. The major difficulty of experimentally tracking the activity of oxygen in the cathode during electrochemical cycling is attributed to the light nature of elemental O and the complex composition of cathode materials.[39,40] For most characterization methods, the weak signals generated by O could be easily affected or covered by other components of cells. Meanwhile, the extreme sensitivity of batteries' components to water and oxygen requires the cell to be detected under *in situ* conditions, which is further limited by the closely packed architecture of cells.

Nevertheless, extensive efforts have been devoted to developing applicative characterization methods in this area.[41–45] Some efficient techniques such as differential electrochemical mass spectrometry (DEMS),[46,47] resonant inelastic X-ray scattering (RIXS),[48,49] magnetism-based techniques,[45,50] and transmission electron microscopy (TEM)[51,52] have been proposed to investigate gas evolution, oxygen chemical changes and

Junrun Feng

Dr Junrun Feng received his PhD from University College London (UCL) in May 2023. He currently joined the Green Battery Innovation Laboratory and became a Lecturer in Hubei University of Technology (HBUT). His research interest mainly focuses on the characterization of electrodes and electrode/electrolyte interfaces in secondary rechargeable battery systems.

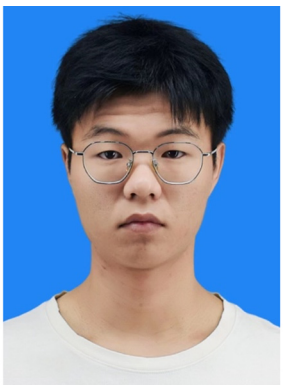

Zhuo Chen

Mr Zhuo Chen received his Bachelor of Engineering from Wuhan Donghu University in June 2022. Then he started to be a master student in Hubei University of Technology under the supervisor of Prof. Zhangxiang Hao and Dr Junrun Feng. His research focuses on electrolyte additives in secondary rechargeable battery systems.

Weihua Zhou

Mr Weihua Zhou received his BS from Hubei University of Technology in June 2021 and now is a research master in Hubei University of Technology. Under the supervision of Prof. Zhangxiang Hao and Dr Junrun Feng, he conducted research on the modification of metal anodes in secondary batteries systems.

Zhangxiang Hao

Prof. Dr Zhangxiang Hao received his PhD from Huazhong University of Science and Technology (HUST). He then worked as a postdoctoral researcher in University College London (UCL) for more than three years. He joined Hubei University of Technology (HBUT) in 2021 and led the Green Battery Innovation Laboratory group, which focuses on batteries of energy storage and conversion.

structural degradation associated with O_2 loss phenomenon. Based on these excellent works, significant progress has been made in the past few years,[53] especially in investigating the origin of oxygen loss in LLMO cathodes and its impacts on structural degradation. This review is focused on the characterization methods used to detect the origin and effects of oxygen loss in LLMO cathodes. We first summarize the recent works that investigate the origin of the oxygen loss in LLMO cathodes. Then, the characterization methods used to detect the phenomenon are categorized by their functional principles and introduced with examples. Finally, we discussed our vision of the current role and prospects of oxygen release in layered cathode studies based on these summaries. The requirement of future characterization methods will also be proposed, with the aim to improve the fundamental understanding of failure of Li-ion batteries and inspiring interest in the future development of layered oxide cathodes.

2. Origins of oxygen evolution in lithium layered oxide cathodes

The most traditional LLMO cathodes are $LiCoO_2$, $LiNiO_2$ and $LiMnO_2$, in which the first two were synthesized by Goodenough *et al.* in the early 1980s[54,55] and the last one was reported by Bruce *et al.* in 1996.[56] The successful development of these cathodes contributed to the commercialization and popularization of rechargeable Li-ion batteries in the 1990s.[57] However, these cathodes show disadvantages such as low capacity, short cycle life and high costs. Advanced systems such as lithium nickel manganese cobalt (NMC) oxides,[58–60] and Ni-,[17,28,61] Li and Mn-rich LLMO cathodes[62–64] have been proposed. Typical examples and their characteristics are provided in Table S1 (ESI†). Although most of the materials have been studied well, they still suffer from safety concerns when charged to high voltages (>4.4 V *vs.* Li^+/Li), which are found to originate from the oxygen loss phenomenon of LLMO cathodes.[65–67]

The major difference in the different categories of LLMO cathodes is the metal cation and its amounts, which affects not only the electrochemical performance, but also their properties related to the oxygen loss phenomenon. For example, $LiCoO_2$ shows a more intensive oxygen loss phenomenon than that of $LiNiO_2$ while comparing the outgassing during the cycling.[68] Voltage hysteresis occurs when charged to high voltages, which is another indicator of the oxygen loss phenomenon and has been associated with the oxygen redox behavior of the LLMO cathode.[64,66] The cathode with more intensive oxygen loss will show a lower voltage of hysteresis and, thus, poor cycling stability. For example, it was found that the higher Ni content of NMC-based LLMO cathodes results in a higher capacity but low voltage of hysteresis.[69] A similar conclusion can also be drawn for Ni-rich cobalt-free LLMO cathodes (Table S1, ESI†).[70] Li- and Mn-rich LLMO cathodes are promising candidates for the next-generation Li-ion batteries due to their high capacity and low cost. However, studies that stated Li- and Mn-rich LLMO cathodes suffer from structural degradation and oxygen release phenomenon during cycling, which is due to the John-Teller lattice distortion introduced by Mn.[10] The variation in the voltage hysteresis of different LLMO cathodes can be explained by the band theory, which will be discussed in Section 2.1. Apart from the electrochemical stability, the gaseous products released and the cathode-electrolyte interface of different cathode-based Li-ion batteries show similar compositions, suggesting that they have similar mechanisms when the electrolyte is involved (Table S1, ESI†). Thermal stability is another factor related to the oxygen loss phenomenon, as the inner temperature of cells will increase during the long-term cycles, which induces the decomposition of LLMO cathodes and release lattice oxygen to the system.[71,72]

On the basis of current knowledge and the above-mentioned discussion, the origins of oxygen loss phenomenon are attributed to three main parts: the state of charge of LLMO cathodes, interfacial reactions between LLMO cathodes and electrolytes, and the thermal instability of LLMO cathodes (Fig. 1). In the following text, these three parts will be discussed in detail.

2.1 State of charge of layered oxide cathodes

The state of charge could be the major driving force of oxygen loss in the LLMO cathode structure.[73–76] During the charging process, the Li-ions will be deintercalated from the cathode structure along with the rise in voltage. The process gradually oxidizes the transition metal ions from 3^+ to 4^+ and makes them more oxidative, so that they become more likely to access the electrons from the lattice oxygen (O^{2-}), which eventually results in the release of gaseous O_2 to the surrounding environment.[77–80] Therefore, a higher voltage could accelerate the oxidation of lattice O^{2-} to gaseous oxygen as stronger extraction of Li^+.[81,82] Such relationship between oxygen loss and the state of charge of LLMO cathodes has been studied and verified by enormous works.[83–87] For example, a $Li_{1.2}Ni_{0.2}Mn_{0.6}O_2$ cathode shows obvious detection of O_2 upon the voltage reaching around 4.5 V *vs.* Li^+/Li and the maximum rate of $\sim 4 \times 10^{-2}$ μmol min^{-1} at 4.8 V *vs.* Li^+/Li.[88] Furthermore, the relationship between the state of charge and oxygen loss is also affected by the composition of LLMO cathodes. A typical comparison is presented by Shao-Horn *et al.*[89] The Li_2RuO_3 cathode was substituted by different metal ions and fabricated into cells. The evolution of gaseous products (CO_2 and O_2) was detected by DEMS during the operation. A distinct difference was observed by comparing the initial time of oxygen evolution and the total amount of oxygen generated (Fig. 2a–d).

The difference suggests the significant influence of LLMO composition on the relationship between the voltage and the oxygen loss phenomenon. Such influence could be explained by the band theory.[88,90] The band structure of LLMO cathodes is considered as orbitals overlapped between the d orbitals of transition metals and the p orbitals of oxygen, resulting in bonding (M–O) and antibonding (M–O)* (Fig. 2e). The energy difference between the two bonds is the charge transfer term Δ, which depends on the electronegativity difference between M and O and will be used later. Normally, all three 2p orbitals of O

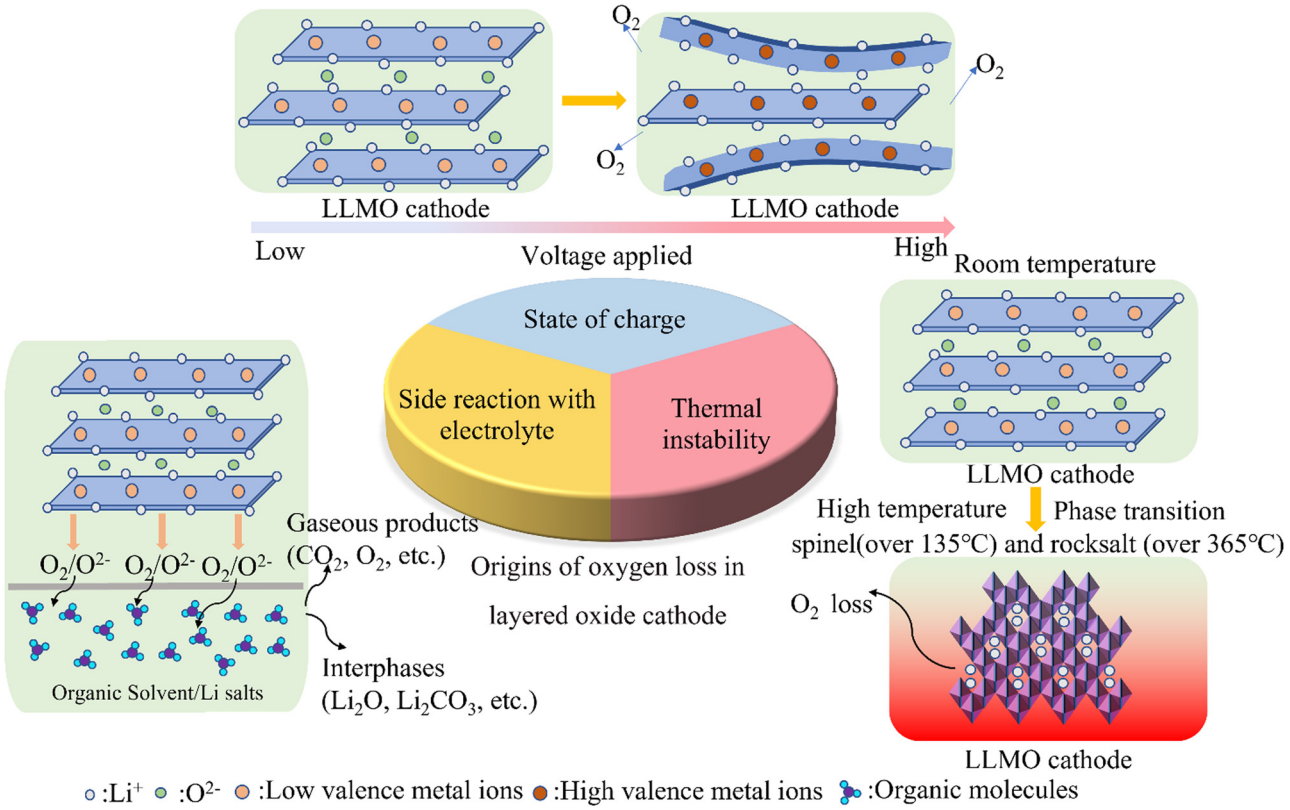

Fig. 1 Origins of oxygen loss phenomenon in LLMO cathodes.

will form a bond with M in $LiMO_2$ when O/M is 2. However, a partial substitution causes changes to the coordination environment between TM and O. For example, Li-rich layered Li_2MO_3 cathodes with one-third of TM replaced by Li result in one of the O 2p orbitals being weakly bonded because of its relatively small overlap with Li 2s orbitals. Thereby, a non-bonding oxygen state is formed and located above the stabilized (M–O) bonding band (Fig. 2f). Such a band can provide additional electrons for removal and thus higher capacities without any risk of structural destabilization. However, it also changes the redox activity when different band positions are considered, possibly inducing the oxygen release in the layered oxide cathode. To be clear, the partially filled (M–O) * band will be split into empty upper and filled lower-Hubbard bands (UHB and LHB, respectively) by Mott–Hubbard splitting. The position of LHB related to the O 2p non-bonding band shows three typical cases (Fig. 2g–i), which are related to the Δ and U (d–d coulomb interaction term, which is inversely proportional to the orbital volume). Ideally, when the LHB is overlapped with the O 2p non-bonding band, both bands are available for electrochemical activity (Fig. 2h). However, when the LHB is lower than the O 2p non-bonding band, the electrons are directly removed from the O 2p non-bonding band (Fig. 2i), which promotes the formation of O_2 and degradation of the cathode. Apart from the influence of composition, the Li-ion cathodes also show a spatial difference of the state of charge within the whole structure. Such inhomogeneous delithiation of LLMO cathodes during cycling has been proven to be another driving factor of oxygen loss by Amine *et al.*[35] The lattice displacement/strain induced by non-equilibrium structural dynamics is observed along with the oxygen loss in Li-and Mn-rich LLMO cathodes during the electrochemical cycles. Such a conclusion is based on a combination of multiscale characterization methods, which will be further discussed in Part 3.

2.2 Side reactions between LLMO cathodes and electrolytes

The side reactions between layered oxide cathodes and electrolytes during the electrochemical cycles are one of the most important phenomena in Li-ion batteries.[91–93] The reaction consumes lithium and oxygen in the cathode, forming gaseous products and solid–electrolyte interfaces at the cathode/electrolyte interface.[94,95] Among the complicated and multi-step interfacial reactions, the major reactions in which the oxygen loss of LLMO cathodes is involved are the reduction of O_2 and the formation of Li_2O and Li_2CO_3-based interfaces.[10,96]

The first reaction is initialized by O_2 released from the lattice structure of LLMO cathodes at high voltages. The oxygen generated is extremely oxidative and can be easily reduced by the carbon black or carbon species in the electrolyte (mechanism 2 in Fig. 3c), producing gaseous products such as CO_2 and CO that can be easily detected by gas detection methods (Fig. 3a).[97–100] The reaction results in the decomposition of electrolytes and induces the interfacial reactions between

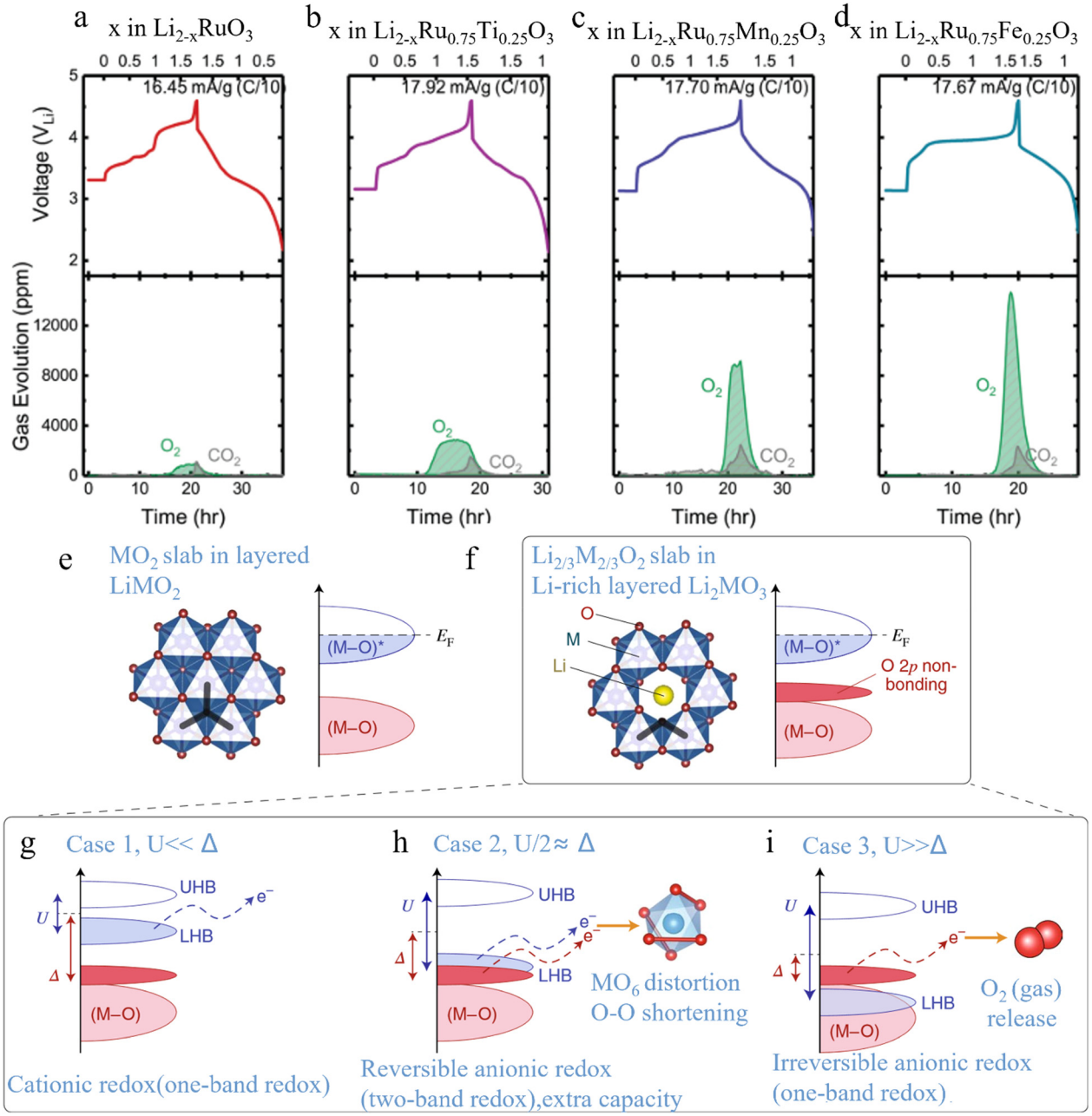

Fig. 2 (a)–(d) Charge and discharge profiles and corresponding concentrations of CO_2 and O_2 detected by DEMS of LLMO cathode-based Li-ion batteries. Copyright 2021, Royal of Chemistry.[89] (e) and (f) Band structures of the layered Li_2MO_3 cathode and its anionic redox mechanism. (g)–(i) Three scenarios of the Hubbard model. Copyright 2018, *Nature*.[90]

electrolytes and LLMO cathodes due to charge compensation (mechanism 1 in Fig. 3c).[10,85] Various by-products in the form of CO_2, CO, O_2, O^{2-}, and H_2O will further participate in and initiate the interfacial reactions at the cathode/electrolyte interface, intensifying the loss of oxygen from cathodes (Fig. 3d).[10,101] The lost oxygen will be preserved at the interface in the form of Li_2O and Li_2CO_3, comprising the cathode-electrolyte interfaces (CEI) (Fig. 3b), which has been extensively studied in various LLMO cathode-based systems.[102–104]

Additionally, the reaction and formation of the CEI significantly changed the charge transfer process in the batteries, resulting in an increase in the local temperature and overpotentials of the cell. This process will accelerate the lattice oxygen loss from the LLMO cathode structure *via* the above-mentioned interfacial reactions.[85]

2.3 Thermal instability of layered oxide cathodes

The thermal instability of layered oxide cathodes also possibly contributes to oxygen loss in layered oxide cathodes.[72,105–107] During cycling, the inevitable exothermic side reaction and electrochemical process could release heat and elevate the temperature inside the cell, which leads to the phase transition

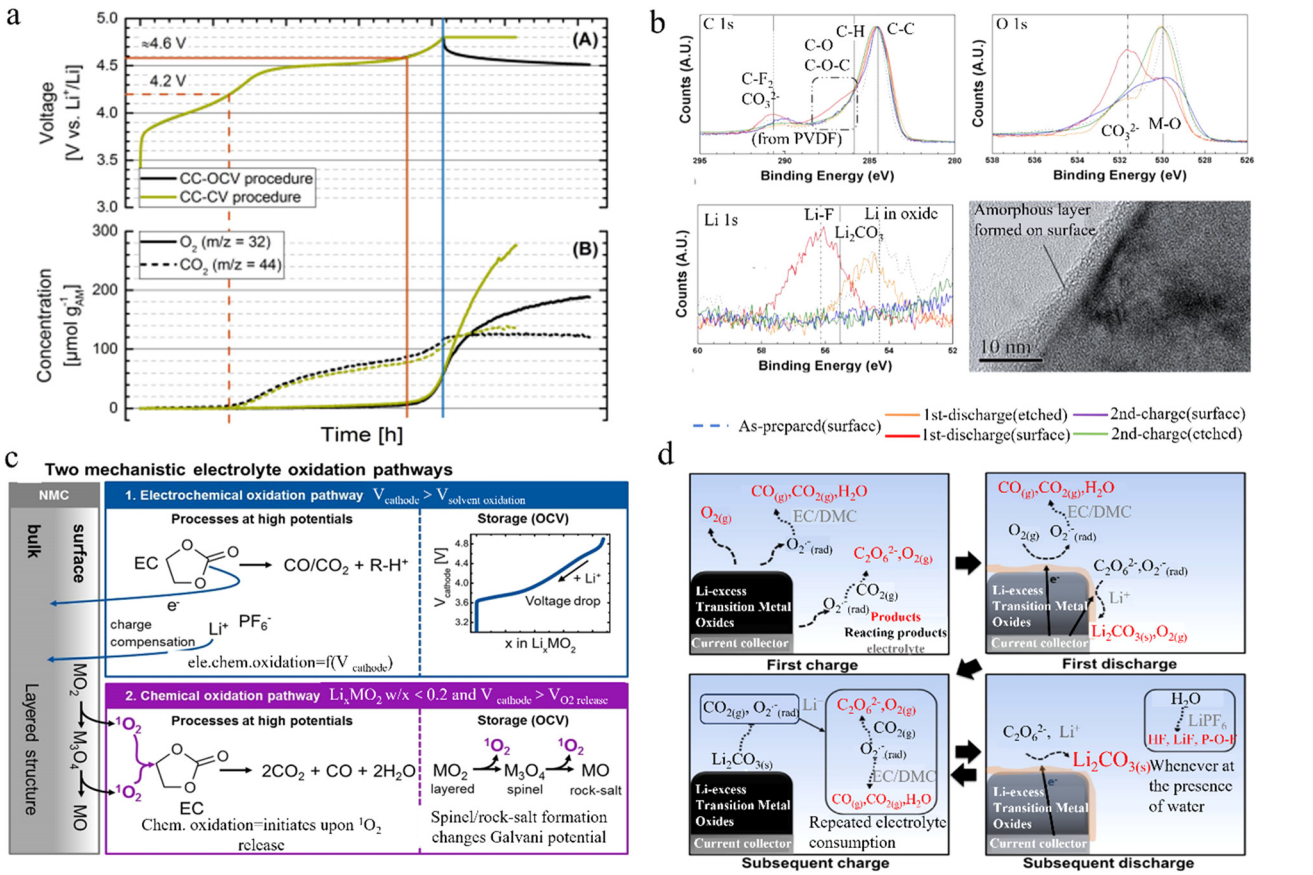

Fig. 3 (a) Voltage *vs.* time curve (top) and the evolved amount of O_2 and CO_2 (bot). Copyright 2017, The electrochemical Society.[27] (b) XPS and high-resolution TEM studies of the surface of Li-rich cathodes at different electrochemical states. Copyright 2012, American Chemical Society.[179] (c) Schematic description of the proposed electrochemical and chemical electrolyte pathways, Copyright 2017, The electrochemical Society.[26] (d) Proposed mechanism of successive reactions of oxygen evolution out of the layered Li-excess metal oxide cathode. Copyright 2012, *American Chemical Society*.[179]

of LLMO cathodes.[10,108] For example, Ni-rich NCM cathode particles were observed to reconstruct at high temperatures and transit to a rock-salt-like structure during heating (Fig. 4a and b).[109] With the increase in temperature to 175 °C, the Ni-rich NCM cathode (NCM85105) particle shows a variation in morphologies, indicating the decomposition and reconstruction of cathode particles and the nanopore evolution at different temperatures (Fig. 4a). With the increase in temperature, the shape of the nanopore boundary changes, suggesting that a transition of phase has occurred as a result of oxygen loss. The transition of phase was confirmed by high-angle annular dark-field (HAADF) imaging techniques (Fig. 4b). The nanopore boundary encounters phase transition from a layered structure to the rock-salt-like structure. Furthermore, the influence of phase transition on the oxygen loss phenomenon of LLMO cathodes was reported by Nam *et al.*[110] The phase transitions of NMC-based LLMO cathodes were recorded *via* time-resolved XRD patterns. X-Ray diffraction is sensitive to the changes in crystal structures in samples, in which the (003) peak represents the layered structure of rhombohedral symmetry ($R\bar{3}m$), while the (220) peak is characteristic of the spinel structure (Fig. 4c).[111] With the help of mass spectroscopy, the relationship between phase transition and oxygen loss was established (Fig. 4d). The oxygen evolution and structural phase change during heating are influenced by the content of Ni and Mn: the higher the Ni content and the lower the Co and Mn content, the lower the onset temperature of the phase transition (thermal decomposition) and more oxygen is released.[10] The oxygen evolution was detected at a temperature between 135 and 155 °C, where the layered structure is transformed to spinel. Later, the disordered spinel of the cathode was then transferred to the rock-salt structure without detection of O_2, which was completed at around 365 °C. A comparison of different compositions of LLMO cathodes shows that the higher the Ni content, the lower the temperature required for the first phase change (layered to spinel) and the transition to the rock-salt, the lower the thermal instability.[112]

Apart from phase transition, the elevated temperature could induce thermal runaway inside the cell, resulting in the full decomposition of cathodes and CEI. The process generates a large amount of gaseous products, propagates and destroys the internal structure of cells in a short time.[107]

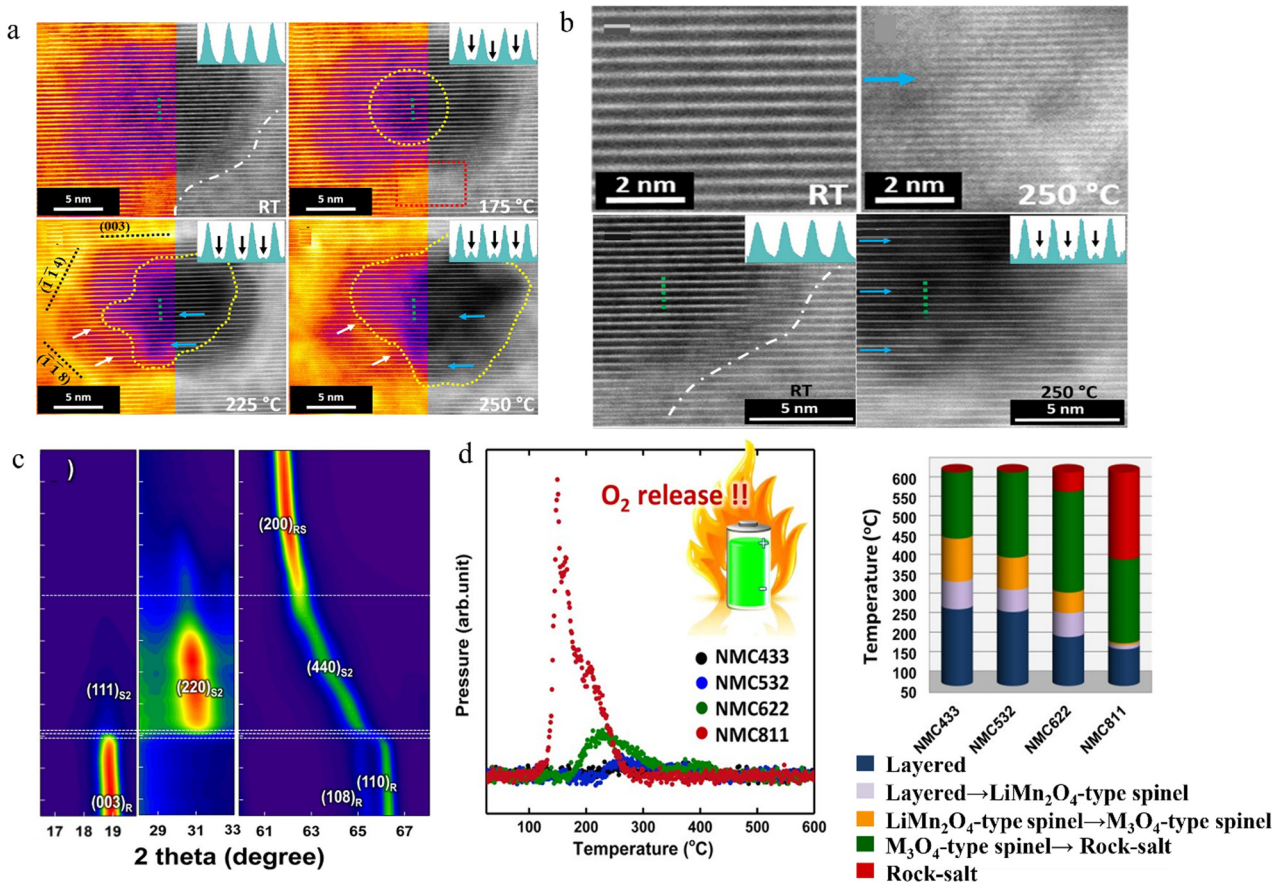

Fig. 4 (a) High-angle annular dark-field (HAADF) micrographs of the nanopore at different temperatures (room temperature, 175 °C, 225 °C and 250 °C). (b) HAADF micrograph in the [210] zone of the same boundary region (top) and the antiphase boundary (bot) at different temperatures. Copyright 2020, American Chemical Society.[109] (c) Time-resolved XRD patterns for the charged NMC811. (d) Mass spectroscopy profiles for oxygen during the measurement of time-resolved XRD. Copyright 2014, *American Chemical Society*.[111]

3. Characterization methods used for revealing the oxygen loss in LLMO cathodes

Despite the complicated process of oxygen loss in LLMO cathodes, the understanding of the phenomenon has been intensively enhanced by developing advanced characterization methods. These methods are widely applicable in this area as the fundamental mechanism of oxygen loss is similar for different types of LLMO cathodes.

In this section, the most widely used methods will be divided based on their functional principles and introduced below, which are gas detection-based techniques, X-ray-based techniques, magnetism-based techniques and other advanced techniques (Fig. 5).

3.1 Gas detection-based techniques

The major final products of oxygen lost from the LLMO cathode are in the form of gases. Therefore, gas analysis for the identification of gaseous products could be the first step to reveal the oxygen release phenomenon. The most commonly used method to analyse gas evolution in electrochemical applications is electrochemical mass spectrometry (EMS). The method was enabled by connecting the hydrophobic porous electrode with the inlet system of a normal mass spectrometer (Fig. 5a). The gaseous products will generate charged fragments of vaporized gaseous molecules by collision with high-voltage electrons. Different species are identified by comparing the time taken by each charged species to reach the detector in a magnetic field, which is related to their m/z ratio. After about 20 seconds, the mass intensity detected was directly proportional to the amount of reactants. The first application of EMS was conducted by Bruckenstein and Gadde in 1971 to determine the O_2 generated from an oxygen-free perchloric acid solution.[113] Later, Wolter and Heitbaum optimized the technique with a hydrophobic membrane (porous PTFE) inlet system that can separate aqueous electrolytes from the vacuum system of the mass spectrometer. The membrane inlet is close to the working electrode and directly connected to an ionization chamber. During the measurement, the gaseous products formed on the electrode can reach the ion source directly, allowing ionization and detection shortly after the generation. Meanwhile, the chamber volume is continuously expanded and produces a mass signal that is proportional to the rate of the incoming flow of gaseous products, which reflects the time derivate of the

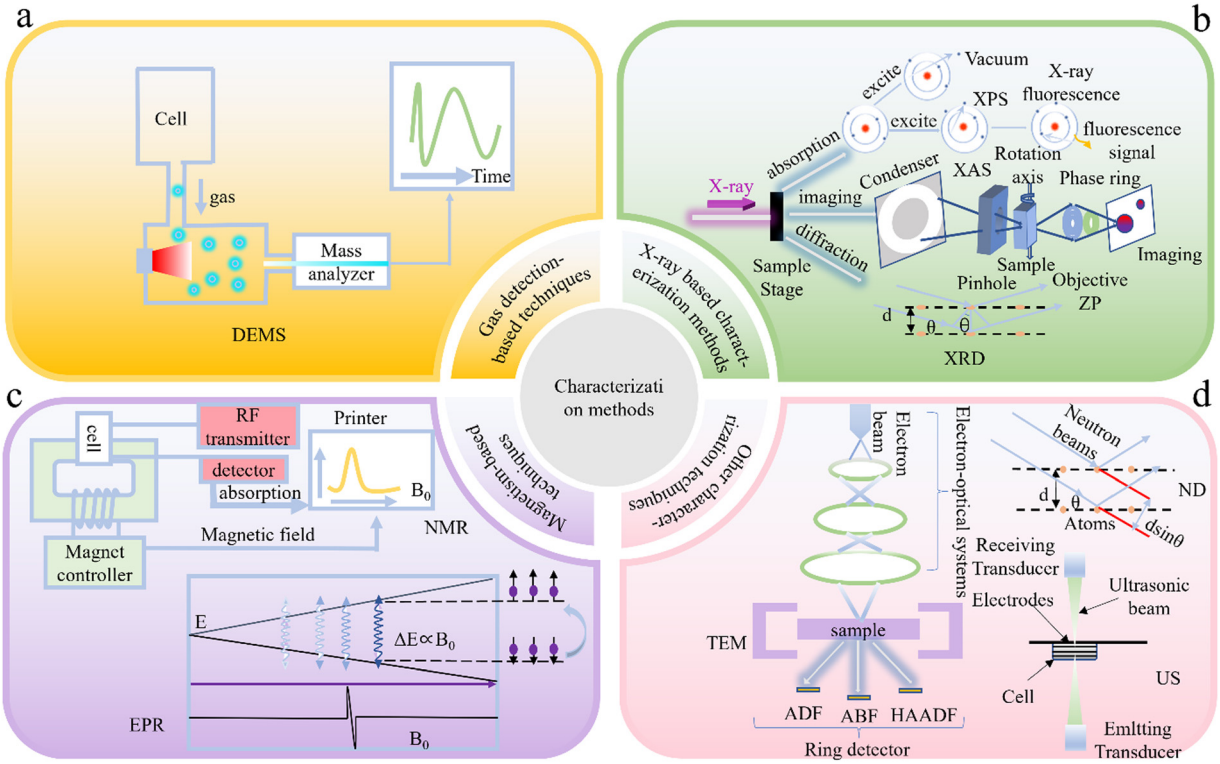

Fig. 5 Characterization methods for testing oxygen loss in batteries: (a) gas detection–based techniques; (b) X-ray-based characterization methods; (c) magnetism-based techniques; and (d) other characterization techniques.

amount of products. Such technique provides higher sensitivity and is called differential electrochemical mass spectrometry (DEMS).[114]

As the oxygen lost in LLMO cathodes during cycling can be released in the form of gases, the detection and identification of these gaseous intermediates and products is a critical step to understanding the process, for which DEMS is a good choice. Currently, *in situ* DEMS measurement is well developed (*e.g.* a typical *in situ* DEMS cell designed by NovaK *et al.* in 2005, Fig. 6a)[115] and used in understanding the oxygen loss phenomenon in different types of Li-ion layered oxide cathodes during the electrochemical measurement.[12,46,116,117] For example, Novák *et al.* used DEMS to study the gas evolution occurring during the first cycles of NMC half-cells under different current densities.[12] Bruce *et al.* demonstrated[118] oxygen loss and associated structural reorganization in a $Li[Ni_{0.2}Li_{0.2}Mn_{0.6}]O_2$ cathode by combination of DEMS and X-ray diffraction, proving the contribution of oxygen and MO_2 formation to the capacity. Such founding explains why Li–Mn–Ni–O compounds show a high capacity of 200 mA h g^{-1} and $LiCoO_2$ only 140 mA h g^{-1}.[119] A similar phenomenon was also observed in other high-energy LLMO cathodes such as Li-rich and Mn-rich cathodes.[88,120,121] However, such a DEMS system is an open system that is more suitable to be used when gas sample flow rates are of the order of 1 mL min^{-1}. The battery system shows a limited gas volume and thus is not very appropriate. Thereby, several online electrochemical mass spectrometer (OMES) systems with semi-closed or closed cell headspaces were designed.[118,122] For instance, Berg *et al.* designed an OEMS setup to study the gas evolution in LCO/graphite cells (Fig. 6b and c), which also enables the monitoring of the partial and total pressure of the cell. The major gases evolved were C_2H_4 (39.1%) and CO_2 (37.2%), which are related to the decomposition of SEI. O_2 gas was detected at a low content of 1.3%, resulting from the release of highly reactive oxygen from LCO.[118]

The application of EMS-based techniques was the first step to investigate the oxygen loss phenomenon of the LLMO cathode. They verified the formation of oxygen-containing gases during the operation. However, these EMS-based techniques provide detection of all gases formed during the operation of the battery, regardless of whether they result from electrodes, electrolytes, or other sources. Additionally, EMS-based techniques distinguish gases by their mass, while the specific chemical, electronic and morphological evolution associated with the gas formation is hard to be probed. To further investigate the role of cathodes in gas evolution, other techniques that can detect the cathode and provide more information are required to be combined.

3.2 X-Ray-based characterization methods

As discussed in Section 2, the oxygen loss is associated with the chemical/electrochemical reaction and phase transition in layered oxide cathodes during the charging/discharging process. Therefore, the detection of chemical and structural evolution is an important part to understand oxygen loss in layered oxide cathodes. With the development of lab-based and

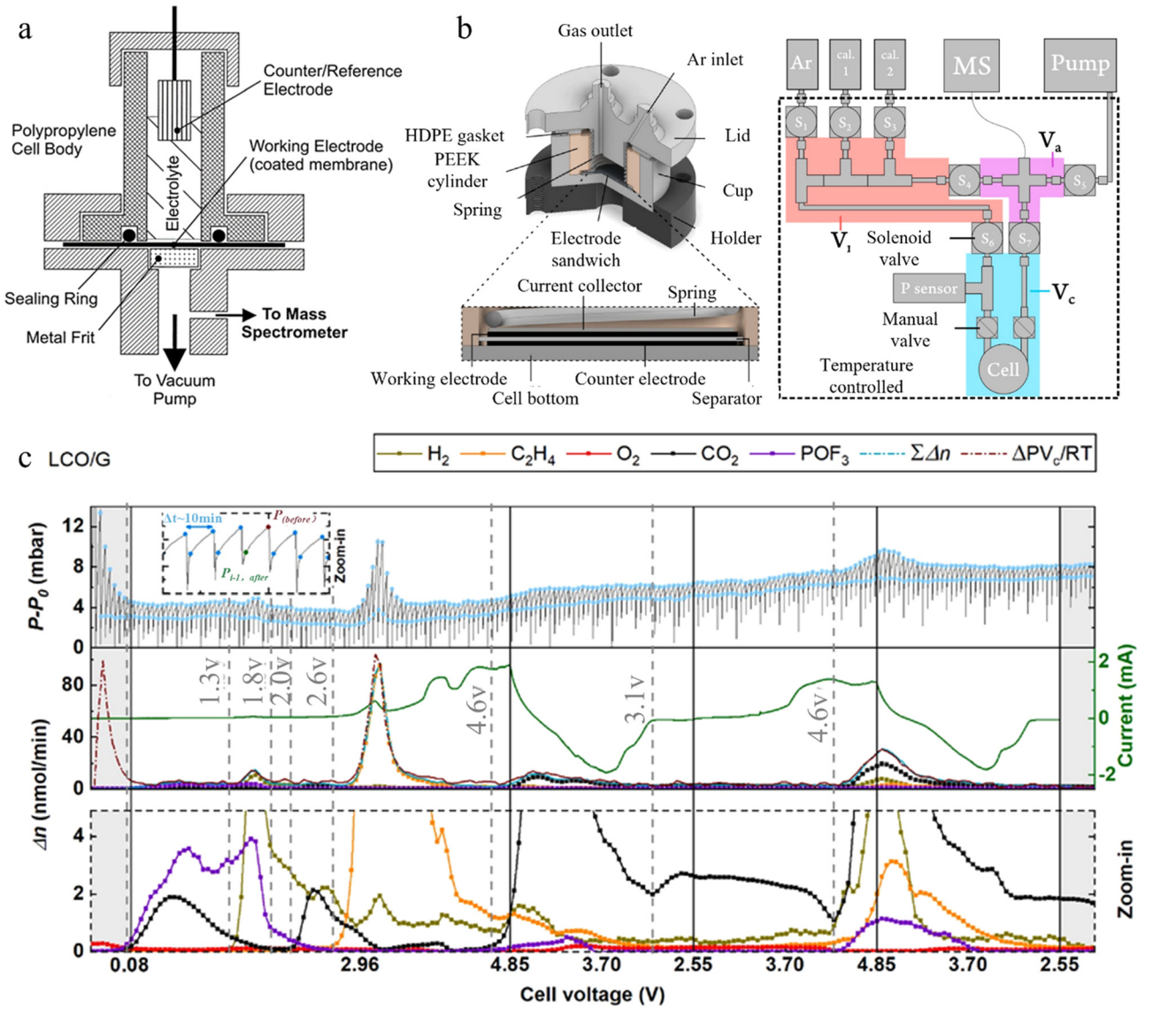

Fig. 6 (a) Illustration of the *in situ* DEMS electrochemical cell. Copyright 2000, Elsevier.[115] (b) Illustration of the electrochemical cell and sampling systems for OEMS. (c) Gas evolution and electrochemical profiles for LCO/graphite cells. Copyright 2021 *Elsevier*.[118]

synchrotron radiation X-ray sources, X-ray beams provide continuously tunable photon energy across a wide range with pertained high brightness and flux, developing numerous characterization methods that are suitable for investigating changes in chemistry, structure, and morphologies of the battery system (Fig. 5b).

With consideration of the penetrating depth, X-rays can be categorized into soft X-rays and hard X-rays. Soft X-rays can only penetrate shallow matters and have a photon energy range of several tens to about 2000 eV. In comparison, hard X-rays have a high energy range of a few keV to tens of keV and a deeper probing ability. In the research on LCO cathodes, both types of X-ray sources are widely used. For instance, X-ray photoelectron spectroscopy (XPS) is a known electron spectroscopy for chemical analysis. During the measurement, the photo will be incident to a sample in the range of X-rays and can activate the electron in the core–shell of atoms from 1 to 10 nm of the material. The electron will be emitted with kinetic energy, which can be detected. Thus, a photoelectron spectrum is recorded by counting ejected electrons over a range of kinetic energies. The energies and intensities of peaks enable the identification and quantification of most surface elements (except hydrogen and helium). XPS can be used to probe the electronic evolution of oxygen during the charge process.[123–126] Rosseinsky *et al.* used XPS to verify that the d^0 cations can stabilize the O–O bond, thereby inhibiting the oxygen loss in the $Li_{4+x}Ni_{1-x}WO_6$ cathode.[125] Gonbeau *et al.* used XPS to reveal the reversible anionic redox chemistry in Li-rich cathodes, while the oxygen loss phenomenon was not focused on.[127] Furthermore, the synchrotron-based X-ray sources allow the application of hard X-ray XPS (HAXPES) to study the depth-dependent oxygen redox acidity in Li-rich layered oxide

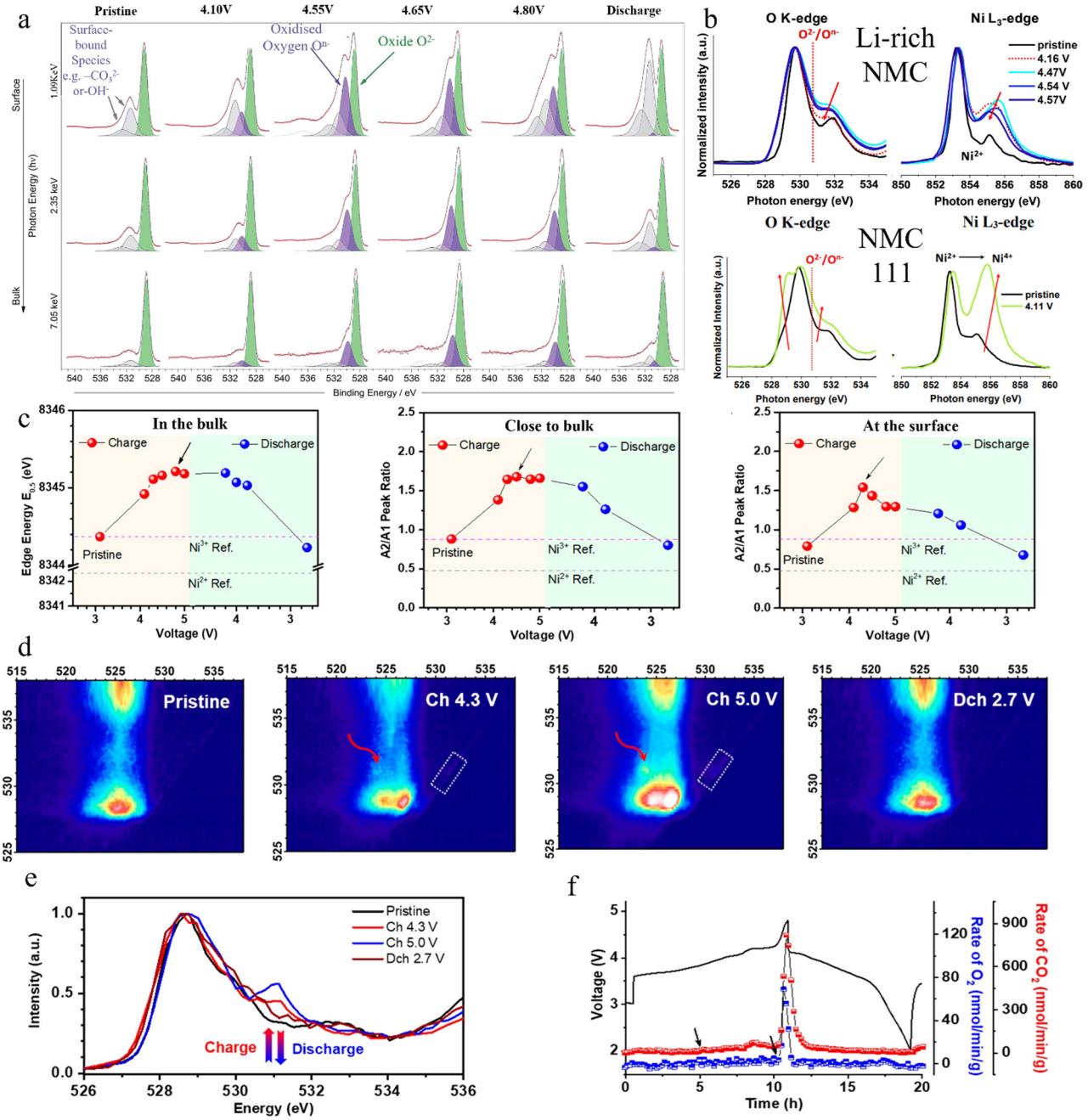

Fig. 7 (a) O 1s HAXPES spectra of $Li_{1.2}Ni_{0.2}Mn_{0.6}O_2$ samples under pristine, charged and discharged status; Copyright 2019, Royal Society of Chemistry.[123] (b) XAS at the O k edge and Ni L3-edges acquired on Li-rich NMC single particles (Top) and NMC111 particles (Bot) at different voltages. Copyright 2019, Wiley-VCH.[33] (c) Corresponding half-edge energy of Ni K-edge XANES at different positions of the $LiNiO_2$ cathode. (d) mRIXS O k-edge mapping of $LiNiO_2$ cathodes during the charge and discharge process. (e) RIX spectra based on the photon intensity upon excitation with an emission energy of 523.7 eV. (f) Gas evolution obtained by DEMS. Copyright 2019, *American Chemical Society*.[28]

cathodes.[123] The O 1s HAXPES spectra (Fig. 7a) show the surface of charged cathode containing more oxidized oxygen O^{n-} than the bulk, indicating a strong depth dependency for the oxidation state of oxygen in the material during charging. Moreover, the proportion of O^{n-} drops slightly at the top of the charge, indicating the oxygen loss from the structure at high voltages.[123] However, XPS/HAXPES requires the sample to be measured under high vacuum conditions, avoiding the absorption from air (oxygen, nitrogen, *etc.*). Such requirement makes the *in situ* experiment hard to realize. Most conclusions were deduced based on *ex situ* experiments, which cannot reflect the realistic condition of battery systems.

In addition to the XPS, X-ray absorption spectroscopy (XAS) is an elemental selective technique used to obtain the electronic structure information on occupied electron states. As oxygen is a light element with a low Z, soft X-rays with a low photon

energy of beams are suitable to study the oxygen loss phenomenon in the layered oxide cathode material. There have been some examples of soft XAS of O kedge reported. However, due to the hybridization between O 2p and the TM d orbital, the valence of oxygen is hard to deduce while the soft X-ray of TM L edge could help. For instance, the effect of O_2 on the surface of the Li-rich NMC cathode could be indicated by Ni L_3-edge. The ratio between the main peak at 853 eV and the shoulder peak at 855 eV is reduced (Fig. 7b) compared to that of NMC 11, which is a result of Ni^{4+} formation, Li-ion removal, and oxygen loss.[33] A more appropriate technique to analyze the O k edge is resonance inelastic X-ray scattering spectrum (RIXS), which is an elemental and orbital-sensitive tool with superior chemical sensitivity. It provides detailed insights into the electronic structure, electronic correlations and a multitude of dynamic processes by varying the excitation photon energy and studying the evolution of X-ray emission spectra.[128] RIXS data can be plotted as a two-dimensional plane, in which X-axis is the incident energy, while the *y*-axis is the energy transfer. The higher dimensionality provides more information than the standard XAS experiment. Some RIXS measurements on layer oxide cathodes have been designed and reported.[34,129,130] Bruce *et al.* used RIXS to investigate the O_2 formation in $Li_{1.2}Ni_{0.13}Mn_{0.54}O_2$ layered cathodes of Li-ion batteries.[131] The formation of short O–O bonds is believed to generate characteristic emission features at 531 eV in the RIXS measurement of O-redox. Along with the voltage hysteresis that occurs during the charging process of the first cycle, O^{2-} was found to oxidize to O_2. Furthermore, the combination of RIXS and other techniques can provide more comprehensive information. Wei *et al.* used *operando* differential electrochemical mass spectrometry, XAS and RIXS to reveal the cationic and anionic redox reactions in the bulk and at the surface of $LiNiO_2$ layered cathodes.[28] Based on the XAS measurement, a different redox activity was observed on Ni in the bulk and at the surface (Fig. 7c), suggesting that the lattice oxygen redox (LOR) occurred. Such a phenomenon was further investigated by the mapping of RIXS (mRIXS) during the charging process (Fig. 7d). Although the mRIXS signals are dominated by strong O^{2-} 2p at around 525 eV emission energy, the signal of O_2 formation (531 eV) is still displayed. The feature starts to emerge when the voltage is over 4.3 V and the intensity increases with the higher voltage. During the discharge, the feature gradually faded and finally disappeared at 2.7 V, showing reversibility (Fig. 7e). RIXS data are also consistent with the gas evolution detected by DEMS (Fig. 7f). The emergence and disappearance of oxidized oxygen provide direct experimental evidence of a lattice oxygen redox. Similar to the XPS, the soft X-ray makes the *in situ* soft-XAS and RIXS measurement difficult to reach. To avoid the contamination of O_2/H_2O, the above-mentioned experiments used an Ar-filled glove box to transfer the sample to the beamline chamber. However, electrodes taken out from cells could induce unwanted changes in chemistry and morphology as the cathode suffers from pressure and electrochemical effects during the operation of cells. Designing a soft X-ray-based *in situ* experiment is urgent to reveal the oxygen redox chemistry in LLMO cathode–based systems. Nevertheless, these spectroscopic techniques are useful to explain the oxygen activation and verify the effectiveness of methods used to optimize the oxygen loss in LLMO cathodes.[34,129–131] For example, Tong *et al.* applied XAS and RIXS to prove that the replacement of Mn with Ru can inhibit the anionic oxygen redox activity in $Li_{1.2}Ni_{0.2}TM_{0.6}O_2$ cathodes.[88]

Apart from the soft X-ray-based characterization methods, the hard X-ray is also commonly used in detecting the oxygen loss of LLMO cathodes. One of the most important applications is X-ray diffraction (XRD), which is a non-destructive technique for analyzing the structure of materials. XRD functions based on the fact that X-rays can interact with the sample and be diffracted, resulting in a pattern of scattering of intensity. By analysing this scattering pattern, the material's orientation, structure, residues and crystalline sizes could be determined. XRD is extensively used to study the relationship between oxygen loss and phase transition in the LLMO cathode during cycling. Some examples were introduced in Section 2.3. Recently, an advanced imaging technique based on X-ray diffraction has been intensively used in battery study, which is Bragg's coherent X-ray diffraction imaging (BCDI). BCDI is mainly used for structural studies of nanocrystals. During each Bragg reflection, the diffraction intensity distribution provides information related to the strain inside the nanocrystal. The major advantage of BCDI is single crystalline component resolution. However, it requires a tiny and compact sample, which could be remedied by the high-energy synchrotron X-ray beam. BCDI can be used to study the displacement in LLMO cathode particles (Fig. 8a and b), at nanometer scales such as NMC811,[24,132] Li-rich manganese-based cathode,[22,133] Li-rich layered oxide cathode,[134] and $LiCoO_2$,[135] which has been proved to be caused by the oxygen release.[35] These findings proved that the crack of electrodes is initiated by strain-stress formed inside the LLMO particles.

Transmission X-ray microscopy (TXM) is another X-ray imaging technique that can provide the chemical evolution of LLMO cathodes with spatial resolution. The working principle is that the X-ray is focused and directed through the pinhole onto the sample. The transmitted X-ray is then amplified by a Fresnel zone and projected onto the detector to form an image. As each element shows different absorption properties of the X-ray, the technique is elemental sensitive and suitable to investigate the inhomogeneous elemental distribution in cathodes. With the variation in energy, the XAS spectra with spatial resolution can also be recorded, revealing spatial effects on the electrochemical/chemical reaction in cathode structures. Moreover, 3D elemental tomography of the electrode or even a single particle (nanometers) can be obtained with the aid of computed modeling and a small beam size. After measuring the 2D X-ray imaging of the sample at a different angle, the 3D image can be generated by processing the series of 2D imaging using a tomographic reconstruction algorithm. The final tomography can reflect both external and internal chemical information of the electrode/particles. For example, TXM combined with XANES spectroscopy was used to directly observe the

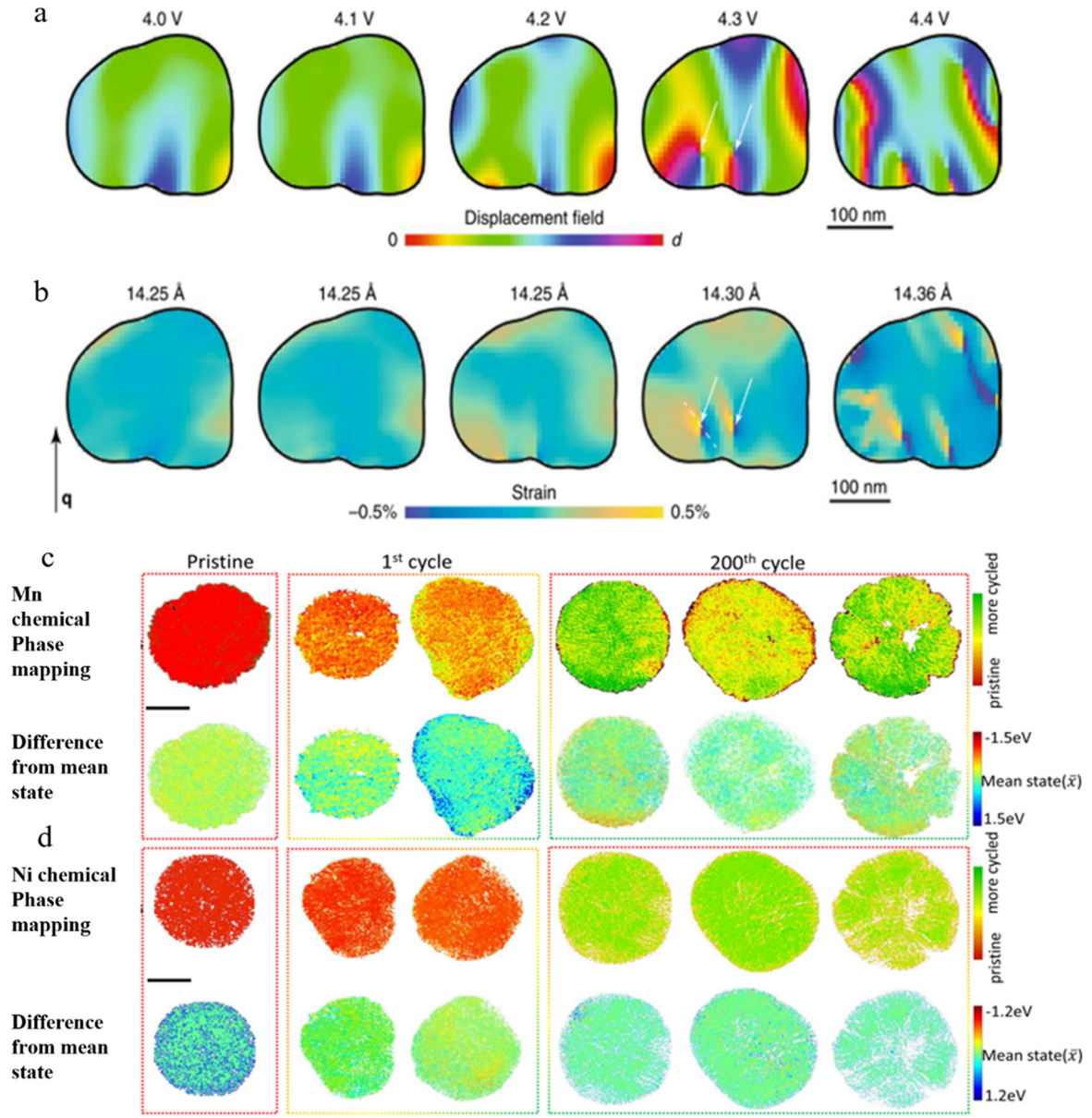

Fig. 8 (a) Change in the displacement of a Li-rich layered oxide cathode nanoparticle. (b) Strain along the (001) direction inside the nanoparticles calculated from (a), Copyright 2018, Nature.[134] (c) and (d) TXM-XANES technique images of Mn and Ni at pristine, 1st cycle, and 200th cycle, respectively, Copyright 2021, Nature.[180]

distribution of Ni and Mn-related chemical phases at the particle level (Fig. 8c and d). The colour changes in the XANES spectrum are caused by changes in the electronic and local structures of the excess metal during cycling. The results indicate that Mn also provides capacity by the redox reaction between Mn^{3+} and Mn^{4+}, while the appearance of a red zone observed at the 200th cycle suggests that the manganese ion reverses to an inactive state. Additionally, mapping reveals cracks existing in the particles during cycling, which along with the decay of electrochemical performance is believed to result from the oxygen loss during cycling. Therefore, gas release in the layered oxide cathode also induces structural changes of the electrode. However, TXM-XANES always requires a long time for data collection, which requires to be measured under *ex situ* conditions or stops the cell at a specific statue for a while, which may affect the accuracy of the conclusion proposed.

In addition to the TXM, X-ray computed tomography (CT) is more suitable to probe the internal part of the battery. The function principle of CT is the attenuation of the X-ray after transmitting the sample. Different materials provide varied attenuation coefficients, so that a different phase contrast can

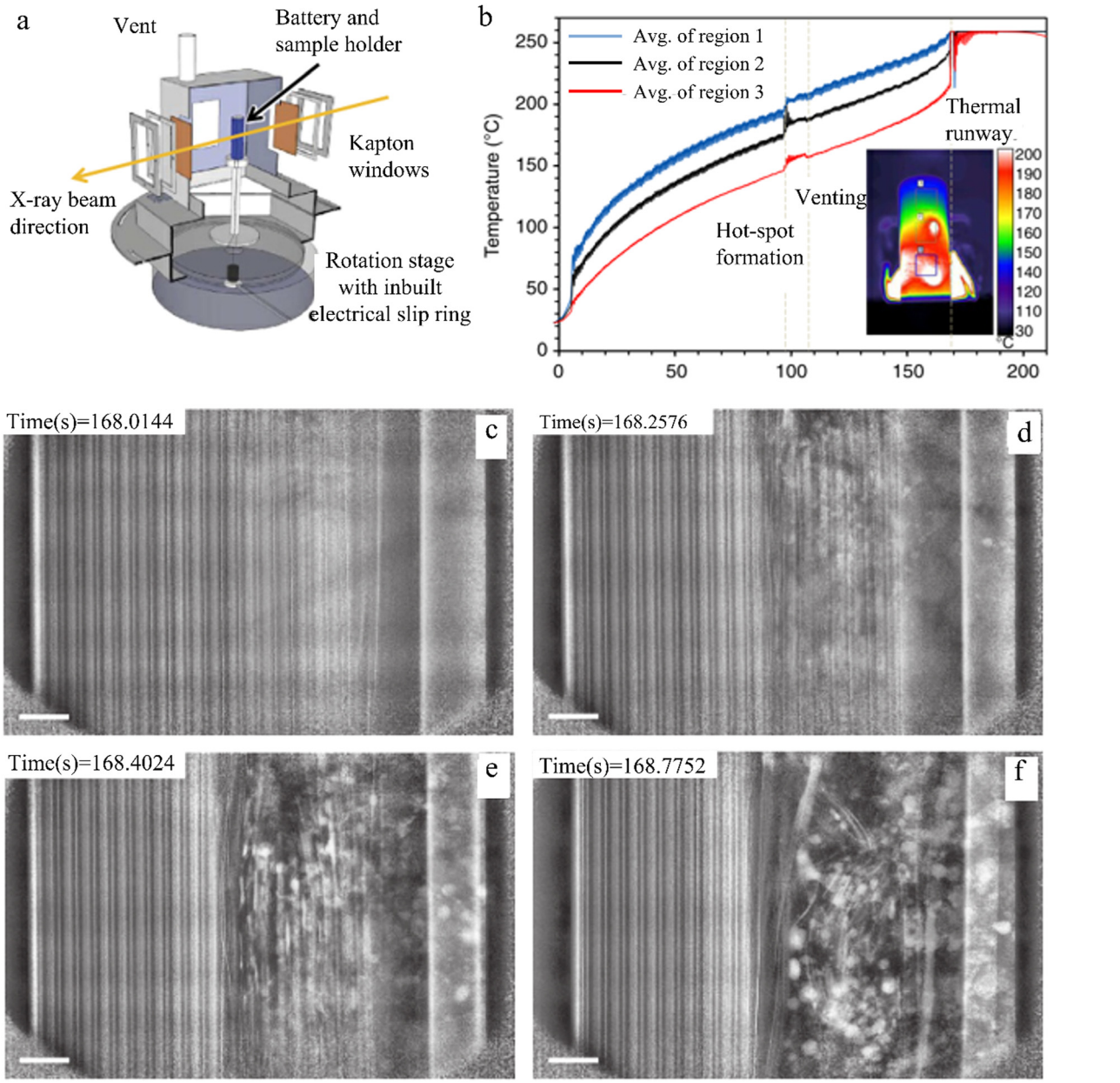

Fig. 9 (a) Schematic diagram of the CT setup. (b) Thermal image after temperature measurement on the battery. (c) Radiograph of the cell before thermal runaway. (d)–(f) Sequential images showing the propagation after thermal runaway on the battery. Copyright 2015 Nature.[107]

be obtained during the measurement. Similar to 3D TXM tomography, 3D CT can be generated to reflect both the external and internal structures of the electrode (Fig. 9a and b). Owing to the development of lab and synchrotron radiation-based X-ray sources, the spatial resolution of X-ray CT can be varied from micro to nano scale, enabling the study of batteries from different scales. X-Ray CT has been widely used to study the effects of gas evolution on the structure of layered oxide-based LIBs under heating conditions and *in situ* electrochemical cycles.[107,136–138] Shearing *et al.* used *in situ* CT with thermal imaging to study the cell architecture evolution as a function of cycle numbers for Li-ion pouch cells.[107] The CT images of the battery before thermal runaway showed a good layer structure (Fig. 9c) but collapsed after thermal runaway (Fig. 9d), which could be observed by combining the thermal measurement. This finding suggests that the cathode material generates gas during the heating-induced decomposition reaction, resulting in a rapid increase in pressure inside the battery and finally damage to the layer structure. However, such a method detects only gaseous products but shows a limitation in distinguishing the composition of gases formed, which could be compensated by coupling with other techniques such as DEMS.

Owing to the high penetrability of hard X-rays, *in situ* XRD, TXM and CT measurements are widely applied in battery studies. Numerous specialized cells and experiments were

designed for allowing the detection of LLMO cathodes by X-rays, which has been well concluded by Yang *et al.*[139] However, these cells and experiments are suitable for micro-probed measurements but not for nano scaled experiments. The nano probed experiments such as nano-TXM, CT, and CDI need the sample to be extremely tiny, requiring to be specially prepared under *ex situ* conditions. Nevertheless, these techniques have made significant contributions to the understanding of the oxygen loss phenomenon of LLMO cathodes, which will be discussed in Section 4.

3.3 Magnetism-based techniques

Magnetism-based analytical tools are used to reveal the change in the local chemical and electronic structural changes in layered oxide cathodes (Fig. 5c). Materials with an odd atomic mass or an odd atomic number show different behaviors in a magnetic field due to their specific spin angular momentum and magnetic momentum. They can be divided into three types: ferromagnetic, paramagnetic, or diamagnetic. Ferromagnetic materials show a permanent magnetic effect even when no magnetic field is applied while diamagnetic materials do not show any magnetic effect even under a magnetic field. In comparison, paramagnetic materials have unpaired electrons or protons, showing no magnetic effect naturally but are responsive to an applied magnetic field. Paramagnetic materials are suitable for nuclear magnetic resonance (NMR) measurements, which help monitor the structural changes over an electrode. NMR occurs when the nuclei of a target atom align to an applied magnetic field, in which the nuclei are induced to change the spin orientation by absorption of energy in the form of a radio frequency wave. The phenomenon generates an oscillating electric field with a definite frequency, which could be further absorbed by the processing nuclei and result in changes in the spin if the radio frequency is similar (so-called 'resonance'). The energy absorbed during the resonance is a function of the nucleus type and reflects its chemical environment in the molecule. In Li-ion battery systems, the most widely used nuclei in NMR are ^{6}Li, ^{7}Li, ^{1}H, and ^{19}F.[140–144] Their high natural abundance provides fast speed and high sensitivity to the structural and chemical changes during charging and discharging, especially useful for detecting the intermediate and short-lived phases. However, to reveal the oxygen environment of the LLMO cathode during cycling, the most suitable type is ^{17}O, which is the only NMR-active nucleus of oxygen. Different from the above-mentioned nuclei, ^{17}O shows a low natural abundance of 0.037%, requiring an enrichment to provide a good signal-to-noise ratio. Such enrichment is expensive and the synthesis of the enriched LLMO cathode is a challenge, which limits the application of ^{17}O NMR in the understanding of the oxygen redox behavior in oxide cathodes.[145] The strongly quadrupolar nature of ^{17}O (nuclear spin $I = 5/2$) also brings difficulties in the practical application of ^{17}O NMR. Even under magic angle spinning, a broad sideband that covers several thousand ppm is commonly observed. Thereby, variable offset cumulative spectroscopy (VOCS) (Fig. 10a) is used to optimize the measurement, instead of the normal single pulse at one receiver offset frequency. The resulting spectrum is generated by overlapping of all slices. The first application was conducted on a $Li_{1.2}Ti_{0.4}Mn_{0.4}O_2$ (LTMO) cathode by Hu *et al.*, which is not the layered oxide cathode but disordered rocksalt.[66] A reversible O redox behavior is observed by ^{17}O NMR and ^{7}Li NMR. However, irreversible loss of Li is also present in the first cycle, which can be explained by the structural degradation induced by oxygen loss and phase transition at high voltages. Later, *ex situ* ^{17}O NMR is applied in $Li_{1.2}Ni_{0.13}Co_{0.54}O_2$ (Li-rich NMC cathode) to study the voltage hysteresis during the first cycle.[131] The ^{17}O NMR spectrum of the Li-NMC cathode at different electrochemical states shows a broadened signal and the authors state the highly paramagnetically shifted environment (3000 ppm) is due to the formation of molecular O_2 in the bulk structure of cathodes (Fig. 10b and c). Very recently, an *in situ* ^{17}O NMR is performed on the Li_2MnO_3 cathode by Urban *et al.*[146] The quadrupolar Carr–Purcell–Meiboom–Gill (qCPMG) is used to enhance the sensitivity and time resolution of measurements,[147] enabling the quantification of O redox activity related to the formation of irreversible O–O bond, SEI and π(Mn–O) complex. The spectrum of the pristine Li_2MnO_3 cathode is shown in Fig. 10d, while the *in situ* results and corresponding electrochemical data are shown in Fig. 10e, and f. Irreversible oxygen loss was observed during the charging process.

Electron paramagnetic resonance (EPR) is another magnetism-based technique based on exciting unpaired electron spin under a magnetic field and providing electromagnetic energy in the range of microwaves, generating absorption spectra. Recently, EPR is becoming popular in the detection of oxygen loss in LLMO cathodes,[14,148–152] especially after Hu *et al.* used EPR to demystify the coexistence of O_2^{n-} and trapped molecular O_2 during the oxygen redox activity of P2-type sodium 3d layered oxide cathodes.[149] Later, similar works have been conducted on LLMO cathode systems.[146,148] For instance, the oxygen redox behavior is revealed by EPR in O_3-type $Li_{1.2}Ni_{0.2}Mn_{0.6}O_2$ and $Li_{1.2}Ni_{0.13}Co_{0.13}Mn_{0.54}O_2$, O_2-type $Li_{1.033}Ni_{0.2}Mn_{0.6}O_2$ and disordered rock salt–type $Li_{1.2}Ti_{0.4}Ni_{0.13}Mn_{0.54}O_2$ cathodes by Liu *et al.*[148] By comparison their scanning EPR spectra (Fig. 11), the formation of O_2 can still be observed in the O_2-type cathode in which out-of-plane transition metal migration is inhibited, indicating that controlling the in-plane disordering in LLMO cathodes could be more effective.

3.4 Other characterization techniques

In addition to the above-mentioned techniques, there are still other characterization methods that have been applied to oxygen loss of LLMO cathodes and show promising potentials in further upgradation (Fig. 5d). Transmission electron microscopy is a valuable analytical tool in materials science. TEM uses electrons as a light source to enhance its resolution to the angstrom level. A high accelerating voltage (80–300 kV) will be used to generate the high-energy electron source, providing the best resolution of 0.05 nm with a magnification of 200 to 1 500 000 times. Such an electron beam will interact with a very

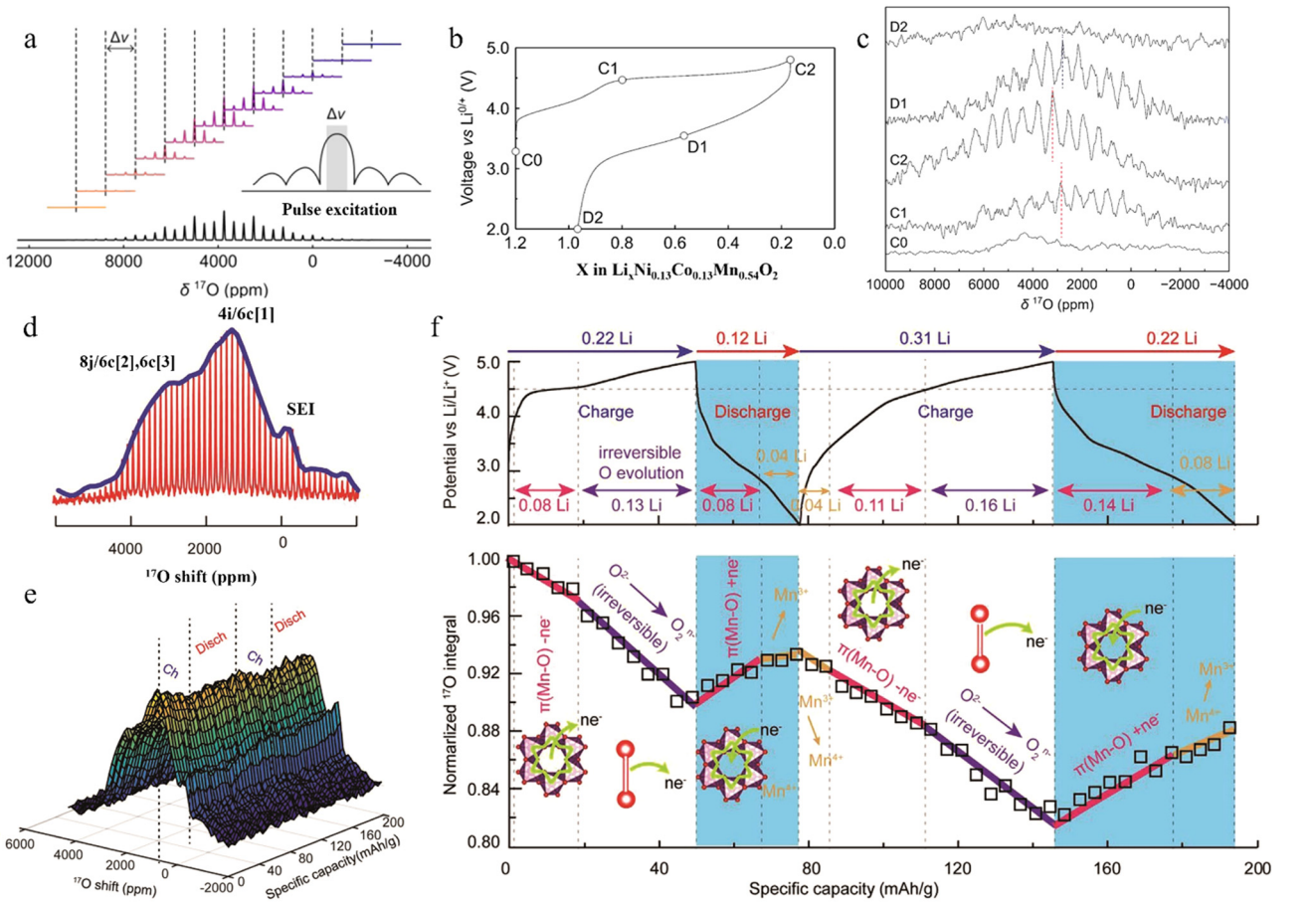

Fig. 10 (a) Illustration of VOCS methods. (b) First charge–discharge cycle of the Li-rich NMC cathode. (c) ^{17}O NMR spectra of the Li-rich NMC cathode under different electrochemical states. Copyright 2022, *American Chemical Society*.[145] (d) and (e) *In situ* 17O NMR spectra of the Li_2MnO_3 cathode in the Li/Li_2MnO_3 cell. (f) Corresponding electrochemical performance and oxygen activity. Copyright 2022, *Wiley*-VCH.[146]

thin sample and give the information from the overall shape to the lattice-level atomic information, enabling the visualization of surface morphology, phase analysis, elemental and compositional analysis. Additionally, techniques such as energy-dispersive X-ray spectroscopy (EDX), electron energy loss spectroscopy (EELS), and high-angle annular dark field (HAADF) can be applied to further analyze the sample, providing more information. Specifically, EDX is a function based on the interaction between electrons and matter, which release X-ray from the core level of the elements. The EELS is another analytical technique from TEM. It can be used to examine the oxidation state of an element by analyzing the absorbed electron energy of the sample. Furthermore, during the penetration of electrons in the sample, some electrons will be absorbed and then diffracted, resulting in a diffraction pattern of the crystal inside the sample. Such signal can be detected using an annular dark-field detector and used to identify the crystallographic growth and detect the defects. In addition to the example discussed in Fig. 4, Zhou *et al.* employed *in situ* TEM to monitor the structural evolution in $LiNi_{0.80}Co_{0.15}Al_{0.05}O_2$ (NCA) induced by oxygen loss during heating under a reducing environment of vacuum.[19] It is stated that oxygen loss undergoes two stages, where the initial stage is a quick process that transforms the cathode surface layer into an amorphized rock salt phase with oxygen vacancies, followed by a slower stage that is along with the recrystallization of the amorphized rock-salt layer *via* coalescing the vacancies. Recently, Amine *et al.* used TEM-based techniques to study the origin of structural degradation in Li-rich layered oxide cathodes ($Li_{1.2}Ni_{0.13}Mn_{0.54}Co_{0.13}O_2$, LMR). The lattice displacement observed by HR-TEM induced by the strain stress occurs on the surface and bulk of the cathode after charging to 4.47 V (Fig. 12a–c).[35] Furthermore, three-dimensional rotation electron reflection (3D-rED, Fig. 12d) examined that the lattice strain triggers transition metal migration and structure transition from the layered phase to the spinel phase (Fig. 12e, f and g). The O k edge EELS line profiles (Fig. 12i) show that the oxygen release uniformly occurs on the whole particle surface as the O pre-peaks disappear, where strain is evolved. The Mn $L_{2,3}$ EELS profile (Fig. 12k) suggests that the Mn oxidation state decreases with migration and oxygen loss near the surface. These findings verified that strain accumulation is the major cause of oxygen release in LLMR. Despite the powerful ability of TEM-based techniques, the damage from the electron

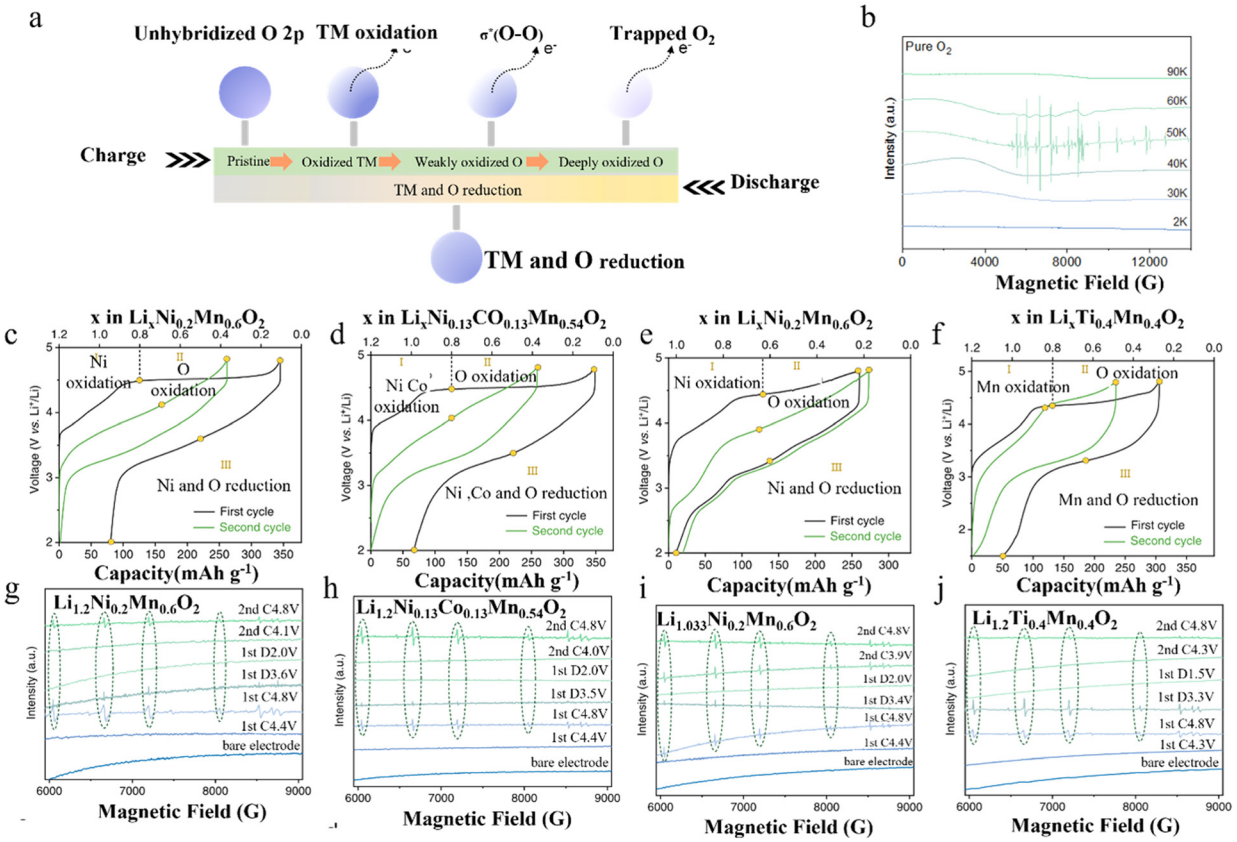

Fig. 11 (a) Illustration of the O redox activity of the LMO cathode during charging and discharging. EPR spectra of (b) pure O_2. Charge and discharge profiles of (c) $Li_{1.2}Ni_{0.2}Mn_{0.6}O_2$, (d) $Li_{1.2}Ni_{0.13}Co_{0.13}Mn_{0.54}O_2$, (e) $Li_{1.033}Ni_{0.2}Mn_{0.6}O_2$, and (f) $Li_{1.2}Ti_{0.4}Ni_{0.13}Mn_{0.54}O_2$. EPR spectra of (g) $Li_{1.2}Ni_{0.2}Mn_{0.6}O_2$, (h) $Li_{1.2}Ni_{0.13}Co_{0.13}Mn_{0.54}O_2$, (i) $Li_{1.033}Ni_{0.2}Mn_{0.6}O_2$, and (j) $Li_{1.2}Ti_{0.4}Ni_{0.13}Mn_{0.54}O_2$. Copyright 2022, *Elsevier*.[148]

beam should be considered and minimized during the measurements.

Neutron diffraction (ND) works on similar principles as XRD (*e.g.*, Bragg's equation), while ND is more sensitive to light elements such as lithium and oxygen and shows better contrast than X-ray-based techniques.[153] It offers local structural information, especially in atomic pair distribution correlating to the intrinsic properties of target materials. Initially, the application of ND in the battery study is difficult due to the existence of hydrogen in every part of the battery, which has a large incoherent neutron-scattering cross-section and detriments the signal-to-noise ratio of the neutron diffraction pattern. The long acquisition time limited by the strength of neutron flux poses significant challenges to ND analysis for the Li-ion battery study under *in situ/operando* conditions. Nevertheless, several special strategies have been developed to overcome these challenges. For instance, Biendicho *et al.* designed a large cell to ensure that enough materials were exposed to the neutron beam.[154] Peterson *et al.* applied deuterated electrolytes to minimize the effects of hydrogen on signal noise.[155] Valdmanis *et al.* used single-crystal (100) Si sheets as casting support materials, improving the signal-to-noise ratio.[156] Currently, ND has been applied to study the phase and volume changes on LLMO cathodes during electrochemical changes such as $LiCoO_2$,[157–159] $LiFePO_4$,[160–163] NMC-based cathodes,[30,164–166] Ni-rich layered oxide cathodes[167] and Li-rich layered oxide cathodes.[168,169] However, works using ND to analyze lattice oxygen evolution in the LLMO cathode are still rarely reported.[77,170] Wang *et al.* studied the variation of O–O pair distance in the bulk of $Li_{1.2}Ti_{0.35}Ni_{0.35}Nb_{0.1}O_{1.8}F_{0.2}$ cathodes during the electrochemical cycling, by measuring O scattering and analysing the atomic-pair coordination.[171] Compared to 2D-ordered cathodes, 3D-disordered cathodes show a steadier framework.

Ultrasonic scanning imaging is an emerging method used in batter systems in recent years (Fig. 13a), with the advantages of an inexpensive cost, convenience, and non-destructive nature.[172,173] It uses high-frequency sound waves to produce images of batteries during the operation of Li-ion batteries. When the ultrasound wave emitted from a focusing transducer passes through the sample, it will be attenuated and then detected by another transducer on the other side (Fig. 13b). The ultrasonic signal collected revealed that the time of flight and amplitude are affected by changes in the physical properties of the material studied. The value of the ultrasonic transmission wave will then transfer into colors and then form the images of cells. During the measurement, a distinct boundary can be observed between different phases such as solid–liquid, solid-gas and gas–liquid interfaces, due to the variation in terms of the ultrasonic attenuate rate (Fig. 13c). Thereby, it

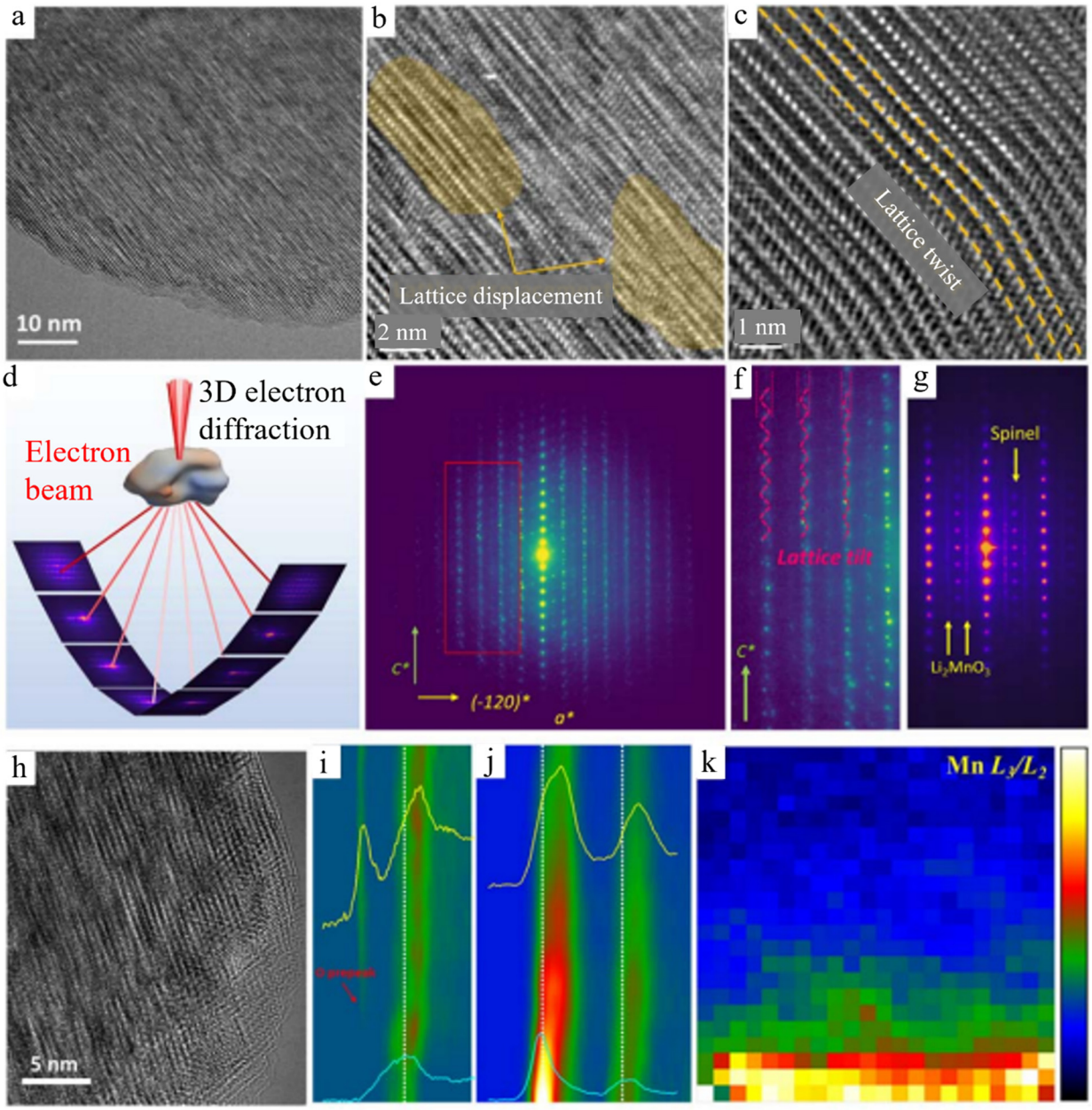

Fig. 12 (a) High-resolution TEM image of LMR at low magnification; (b) enlarged image of the LRM particle; (c) high magnification; (d) illustration of data collection process of 3D-Red; I 3D-Red image along the *a** axis of LMR cathode particle; (f) enlarged image of (e); (g) SAED image of the LMR cathode particle charged to 4.5 V; (h) low-magnification TEM image of the LMR cathode charged to 4.8 V; (i) EELS of the O k edge of the LMR cathode particle charged to 4.8 V; (j) EELS of Mn L2,3 edge of the LMR cathode particle charged to 4.8 V; (k) 2D EELS mapping of Mn L2,3 edge, in which red represent lower valence states of Mn while blue represent higher valence states. Copyright 2022, *Nature*.[35]

can be used to detect gas generation in Li-ion batteries during the operation. Shen *et al.* tested the NMC532/artificial graphite cell, and gases are observed in the ultrasonic image when the cell charged to 4.1 V for 2500 cycles (Fig. 13d).[174]

4. Summary and perspectives

Oxygen loss in the LLMO cathode is proven to be one of the major driving forces of cell degradation. The phenomenon could induce phase transition, strain–stress accumulation, side reactions between electrolytes and safety concerns when combined with the thermal runaway. It is believed that inhibiting the oxygen release could be one of the most effective strategies of optimizing the cycling stability of LLMO cathode-based Li-ion batteries, which requires a deeper understanding of its origins and impact on the LLMO cathodes' properties. Oxygen release could be initiated by the state of charge (or high voltage applied) and intrinsic thermal instability of the structure. Later, the released oxygen will participate in the reaction between the

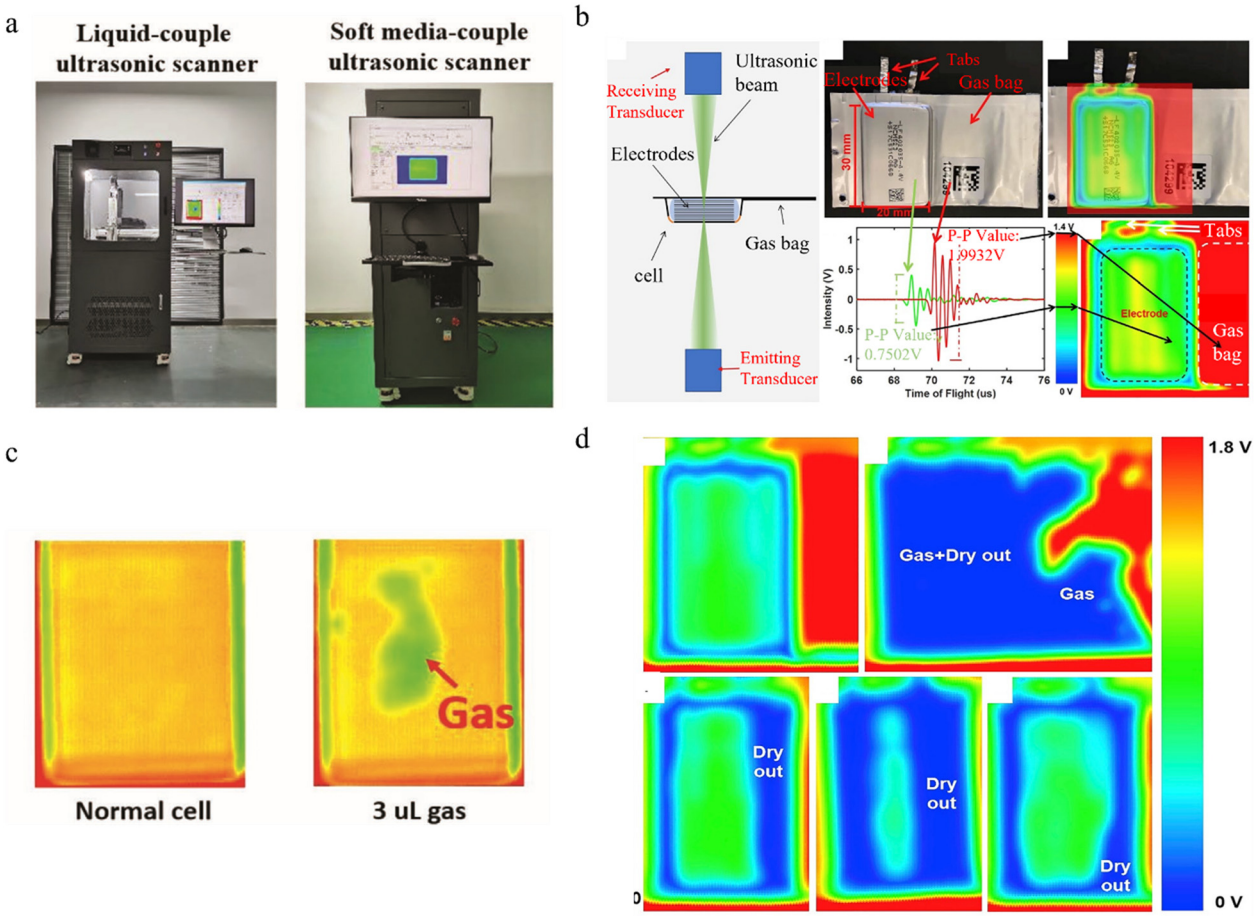

Fig. 13 (a) Photos of the ultrasonic scanner machine; Copyright 2020, WILEY-VCH.[173] (b) Illustration of the principle of the ultrasonic scanning instrument. (c) Ultrasonic imaging of the normal cell and cell with gases. (d) Ultrasonic imaging of the cell under (from left to right, top to bot): fresh states; charged to 4.1 V for 2500 cycles before degassing; after degassing; charged to 4.2 V; and charged to 4.3 V. Copyright 2020, *Elsevier*.[174]

cathode and the electrolyte, intensifying further oxygen loss from cathode structures. Therefore, oxygen loss is a complex process driven by multi-factors. To understand such a complex process, advanced characterization methods providing information related to chemical, structural and morphological changes are required, especially under *in situ*/*operando* conditions. In this review, the most characterization methods used to investigate the oxygen loss phenomenon in LLMO cathodes are introduced with examples. These highlighted methods play an important role in the development of stable LLMO cathodes. Their main achievements of understanding the oxygen loss phenomenon of the LLMO cathodes are summarized in Table S2 (ESI†), with derivate modification methods and improved examples. For instance, XAS and XPS techniques revealed that the side reaction between the cathode and the electrolyte enhanced the oxygen loss from the cathode structure.[101,107–109] Noked *et al.* coated an alkylated $Li_xSi_yO_z$ layer onto a Li-rich layered oxide cathode, inhibiting the reaction and reducing the oxygen release during the operation, resulting in a better capacity retention of 81.4% after 200 cycles at a cycling rate of C/3.[175] Cho *et al.* synthesised a stable spinel Li-Mn–O shell outside the layered Ni-rich cathode, showing a high reversible capacity of 200 mA h g^{-1} and 95% capacity retention under severe test conditions of 60 °C. TXM, X-ray CT, and CDI techniques revealed that structural degradation is normally observed along with the oxygen loss phenomenon under thermal treatment and cycling. Doping and cationic substitution of Li sites by monovalent or divalent dopant elements has been widely used to improve the stability. Mg^{2+} was doped into Li sites of Li-rich Mn-based cathodes by Zhao *et al.*[176] The methods built a stronger Li–O–Mg bond that shows a higher thermal stability, an enhanced specific capacity of 305.3 mA h g^{-1} at 0.1C and a better cycle life. However, there is still a need for progress. Recently, Amine *et al.* have used CDI, TEM and EELS and stated that the heterogeneous nature of Li-rich LLMO cathodes inevitably causes pernicious phase displacement/strain, which cannot be eliminated by conventional doping and coating methods.[35] The synthesis of materials with a ribbon superstructure in the transition metal layers could be a possible solution that suppresses migration of the transition metal.[10,34] There are some excellent reviews that are recommended for reading, which conclude the strategies used to inhibit the oxygen loss phenomenon in LLMO cathodes.[18,177,178]

Table 1 Characteristics of characterization methods

Methods	Detection depth	Information detected	*In situ*/*operando*	Spatial resolution	Data collection time	Limitations
DEMS/OEMS	Entire cell	Gas composition	Yes	—	0.1–2 seconds	The origin of gas products is not straight-forward
XPS/HAXPES	Several nanometers at the top surface	Surface chemical evolution	No	—	Seconds–minutes	Surface sensitive only
Soft-XAS	1–500 nm dependent on the mode used	Surface chemical evolution	No	—	Seconds–minutes	Surface sensitive only
mRIXS	Hundreds nm to μm s	Bulk chemical evolution	No	nm to μm	Seconds	Expensive, high requirement of operation
Hard-XAS	Entire cell	Bulk chemical evolution	Yes	nm to μm	Seconds–minutes	Only for heavy elements
XRD	Entire cell	Bulk crystal structure	Yes	nm to μm	Seconds–minutes	Reflect structure information only
CDI	nm s	Bulk crystal structure	Yes	Tens of nm	Seconds–minutes	Expensive, high requirement of operation
X-Ray CT	Entire cell	Structure and morphologies	Yes	~10 μm	Seconds–hours	Nonchemical information provided
TXM	Tens nm	Bulk chemical evolution	Yes	20–30 nm	Minutes–hours	Long data collection time
NMR	cm s	Electronic structure	Yes	—	Seconds–minutes	Poor signal to noise, expensive
EPR	nm s	Electronic structure	Yes	—	Seconds–minutes	Samples with unpaired electrons only
TEM	nm s	Chemistry, crystal structure, morphology	Yes	nm	Seconds–minutes	Sample preparation, beam damage during operation
ND	μm s	Bulk crystal structure	Yes	nm to mm	Seconds–hours	Beam sources are limited, a large number of samples required
Ultrasonic scanning	Entire cell	Gas formation	Yes	mm	Several milli seconds	Hard for qualitative analysis

The characteristics of each method are summarized in Table 1. With enormous efforts, most characterization methods have realized the *in situ* measurements. However, analytical tools with different functional principles can provide only limited information. For instance, XRD only shows structure evolution while XAS indicates the chemical changes. Additionally, the lack of spatial resolution could be a major drawback of most characterization methods. Thereby, to reveal the full picture of the morphology, chemistry, electrochemistry, and kinetics of oxygen loss, combining the different analytical techniques could be a more desirable approach. Some successful combination has been developed and proved to be effective, such as DEMS with BCDI, DEMS with TXM, and DEMS with X-ray CT. However, other combinations could be limited by the variation in the temporal and spatial resolution of these techniques, making the asynchronous experiments difficult to reach, even under the same electrochemical conditions. The rational design of the *operando* experiment with multiple characterisation methods is still required to be developed. However, a one-step *operando* approach is an alternative choice. There have been some works, on the basis of high-resolution TEM-based techniques, yielding comprehensive information related to oxygen evolution under the heating condition. Nevertheless, the beam damage caused by electrons and the critical requirements of sample preparation also affect the experiment during electrochemical cycles.

In conclusion, the oxygen loss phenomenon has attracted tremendous attention toward its critical importance in improving the performance of LLMO cathodes. On the basis of this understanding, four perspectives of understanding oxygen loss in LLMO cathodes are discussed below:

(1) Although the gaseous emissions from the operation of LLMO-based Li-ion batteries have been well monitored by gas analysis tools, a fundamental understanding of the gassing analysis results is not straightforward. It is still hard to trace the origins of emitted gaseous products, is it from electrolyte decomposition or the electrodes? Additionally, as the cell is huge and complicated, the spatial effects should also be considered during the gas emission. Currently, there are some useful combinations between EMS-based technologies and X-ray imaging methods such as BCDI, TXM and high-resolution X-ray CT for providing comprehensive information with spatial resolution. In future research, one-step *operando* techniques such as TEM holder based-specialized cells with gas analysis could be promising.

(2) Chemical evolution during the oxygen loss of LLMO cathodes has been investigated by numerous analytical tools. However, direct and accurate detection of the phenomenon is still hard to reach due to the lightness of oxygen and the blockage from battery cases. Soft X-ray-based techniques show the ability to monitor oxygen evolution while the *in situ*/*operando* measurements are difficult because most of them are only surface sensitive. On the contrary, the hard X-ray with high photon energy shows the ability to penetrate the whole cell. They are only functioned to the K edge of heavy elements such as transition metals (*e.g.* Fe, Ni, and Co), thereby analyzing chemical changes in oxygen, which is not straightforward. Currently, the development of RIXS and ^{17}O NMR is showing

their potential in probing the oxygen redox chemistry in LLMO cathodes during the operation of batteries. Moreover, growing activity in the area is expected along with the development of four-generation synchrotron X-ray sources worldwide.

(3) Another question is the role of oxygen vacancies in the phase transition of LLMO cathodes. Based on the thermodynamic studies, higher concentrations of oxygen vacancies could increase the Li^+ ion mobility, inducing the reduction of the energy barrier from $R\bar{3}m$ lattice to $Fm\bar{3}m$ rock-salt. Experimental evidence of such process realized by techniques such as high-resolution TEM and BCDI could be useful and more convictive.

(4) Finally, the most of the above-mentioned techniques are based on large-scale facilities such as synchrotron radiation. It is expensive and shows limited accessibility. Therefore, the investigation and development of simple and low-cost characterization methods are very important in the area.

Author contributions

During the preparation of the review, Dr Junrun Feng write the manuscript under the supervision of Prof. Zhangxiang Hao. Mr Zhuo chen and Mr Weihua Zhou helped summary publications and proofread the article.

Conflicts of interest

The authors declare no conflict of interest.

Acknowledgements

This work was funded by the Startup fund at Hubei University of Technology, and High-level talent grant of Hubei province.

Notes and references

1 B. Scrosati, *J. Electrochem. Soc.*, 1992, **139**, 2776–2781.
2 R. Koksband, J. Barker, H. Shi and M. Y. Saidi, *Solid State Ionics*, 1996, **84**, 1–21.
3 D. Aurbach, Y. Ein-Eli, O. Chusid (Youngman), Y. Carmeli, M. Babai and H. Yamin, *J. Electrochem. Soc.*, 1994, **141**, 603–611.
4 D. Guyomard and J. M. Tarascon, *J. Electrochem. Soc.*, 1992, **139**, 937–948.
5 Y. Su, Q. Zhang, L. Chen, L. Bao, Y. Lu, S. Chen and F. Wu, *J. Energy Chem.*, 2022, **65**, 236–253.
6 G. Qian, J. Wang, H. Li, Z. F. Ma, P. Pianetta, L. Li, X. Yu and Y. Liu, *Natl. Sci. Rev.*, 2022, 9.
7 K. Dai, J. Wu, Z. Zhuo, Q. Li, S. Sallis, J. Mao, G. Ai, C. Sun, Z. Li, W. E. Gent, W. C. Chueh, Y. de Chuang, R. Zeng, Z.-X. Shen, F. Pan, S. Yan, L. F. J. Piper, Z. Hussain, G. Liu and W. Yang, *Joule*, 2019, **3**, 518–541.
8 J. Wang, H. Kim, H. Hyun, S. Jo, J. Han, D. H. Ko, S. Seo, J. Kim, H. Kong and J. Lim, *Small Methods*, 2020, **4**, 1–30.
9 E. Flores, P. Novák and E. J. Berg, *Front. Energy Res.*, 2018, **6**, 1–16.
10 H. Zhang, H. Liu, L. F. J. Piper, M. S. Whittingham and G. Zhou, *Chem. Rev.*, 2022, **122**, 5641–5681.
11 S. Hu, A. S. Pillai, G. Liang, W. K. Pang, H. Wang, Q. Li and Z. Guo, *Li-Rich Layered Oxides and Their Practical Challenges: Recent Progress and Perspectives*, Springer, Singapore, 2019, vol. 2.
12 E. Castel, E. J. Berg, M. El Kazzi, P. Novák and C. Villevieille, *Chem. Mater.*, 2014, **26**, 5051–5057.
13 S. S. Zhang, *Energy Storage Mater.*, 2020, **24**, 247–254.
14 Y. Y. Wang, Y. Y. Wang, S. Liu, G. R. Li, Z. Zhou, N. Xu, M. T. Wu and X. P. Gao, *Energy Environ. Mater.*, 2021, 1–10.
15 J. Gao, S. Q. Shi and H. Li, *Chin. Phys. B*, 2016, **25**(1), 018210.
16 M. Gao, H. Li, L. Xu, Q. Xue, X. Wang, Y. Bai and C. Wu, *J. Energy Chem.*, 2021, **59**, 666–687.
17 J. Kasnatscheew, M. Evertz, B. Streipert, R. Wagner, S. Nowak, I. Cekic Laskovic and M. Winter, *J. Power Sources*, 2017, **359**, 458–467.
18 S. Sharifi-Asl, J. Lu, K. Amine and R. Shahbazian-Yassar, *Adv. Energy Mater.*, 2019, **9**, 1–19.
19 H. Zhang, B. M. May, F. Omenya, M. S. Whittingham, J. Cabana and G. Zhou, *Chem. Mater.*, 2019, **31**, 7790–7798.
20 J. M. Lim, D. Kim, Y. G. Lim, M. S. Park, Y. J. Kim, M. Cho and K. Cho, *ChemElectroChem*, 2016, **3**, 943–949.
21 Y. Xie, S. Meng, X. Chen, X. Liang, Y. Jin and L. Xiang, *J. Colloid Interface Sci.*, 2021, **594**, 485–492.
22 W. Hua, S. Wang, M. Knapp, S. J. Leake, A. Senyshyn, C. Richter, M. Yavuz, J. R. Binder, C. P. Grey, H. Ehrenberg, S. Indris and B. Schwarz, *Nat. Commun.*, 2019, **10**, 1–11.
23 Y. Zhang, G. Xia, J. Zhang, D. Wang, P. Dong and J. Duan, *Appl. Surf. Sci.*, 2020, **509**, 145380.
24 X. Liu, X. Zhou, Q. Liu, J. Diao, C. Zhao, L. Li, Y. Liu, W. Xu, A. Daali, R. Harder, I. K. Robinson, M. Dahbi, J. Alami, G. Chen, G. L. Xu and K. Amine, *Adv. Mater.*, 2022, **34**(4), 2107326.
25 M. Jiang, G. Qian, X. Z. Liao, Z. Ren, Q. Dong, D. Meng, G. Cui, S. Yuan, S. J. Lee, T. Qin, X. Liu, Y. Shen, Y. S. He, L. Chen, Y. Liu, L. Li and Z. F. Ma, *J. Energy Chem.*, 2022, **69**, 16–25.
26 R. Jung, M. Metzger, F. Maglia, C. Stinner and H. A. Gasteiger, *J. Electrochem. Soc.*, 2017, **164**, A1361–A1377.
27 B. Strehle, K. Kleiner, R. Jung, F. Chesneau, M. Mendez, H. A. Gasteiger and M. Piana, *J. Electrochem. Soc.*, 2017, **164**, A400–A406.
28 N. Li, S. Sallis, J. K. Papp, J. Wei, B. D. Mccloskey, W. Yang and W. Tong, *ACS Energy Lett.*, 2019, **4**, 2836–2842.
29 K. J. Carroll, D. Qian, C. Fell, S. Calvin and G. M. Veith, *Phys. Chem. Chem. Phys.*, 2013, **15**, 11128–11138.
30 L. Geng, J. Liu, D. L. Wood, Y. Qin, W. Lu, C. J. Jafta, Y. Bai and I. Belharouak, *ACS Appl. Energy Mater.*, 2020, **3**, 7058–7065.
31 X. Feng, S. Zheng, X. He, L. Wang, Y. Wang, D. Ren and M. Ouyang, *Front. Energy Res.*, 2018, **6**, DOI: **10.3389/fenrg.2018.00126**.

32 T. Li and Y. Jiao, *Int. J. Electrochem. Sci.*, 2022, **17**, 221030.
33 D. Leanza, M. Mirolo, C. A. F. Vaz, P. Novák and M. El Kazzi, *Batter. Supercaps*, 2019, **2**, 482–492.
34 R. A. House, U. Maitra, M. A. Pérez-Osorio, J. G. Lozano, L. Jin, J. W. Somerville, L. C. Duda, A. Nag, A. Walters, K. J. Zhou, M. R. Roberts and P. G. Bruce, *Nature*, 2020, **577**, 502–508.
35 T. Liu, J. Liu, L. Li, L. Yu, J. Diao, T. Zhou, S. Li, A. Dai, W. Zhao, S. Xu, Y. Ren, L. Wang, T. Wu, R. Qi, Y. Xiao, J. Zheng, W. Cha, R. Harder, I. Robinson, J. Wen, J. Lu, F. Pan and K. Amine, *Nature*, 2022, **606**, 305–312.
36 Z. Wang, S. Huang, B. Chen, H. Wu and Y. Zhang, *J. Mater. Chem. A*, 2014, **2**, 19983–19987.
37 Y. Zhu, H. Pham and J. Park, *ACS Appl. Mater. Interfaces*, 2019, **11**, 38719–38726.
38 N. L. Wu, Y. T. Weng, F. S. Li, N. H. Yang, C. L. Kuo and D. S. Li, *Prog. Nat. Sci.: Mater. Int.*, 2015, **25**, 563–571.
39 G. Xiao, R. Lu, J. Liu, X. Liao, Z. Wang and Y. Zhao, *Nano Res.*, 2022, **15**, 3073–3081.
40 F. Y. Chen, Z. Y. Wu, Z. Adler and H. Wang, *Joule*, 2021, **5**, 1704–1731.
41 R. L. Yongli He, *2D Mater.*, 2020, 0–6.
42 A. Garg, S. Singh, W. Li, L. Gao, X. Cui, C. T. Wang, X. Peng and N. Rajasekar, *Int. J. Energy Res.*, 2020, **44**, 9513–9526.
43 L. Feng, Z. Chen, R. Chen and S. J. Dillon, *J. Power Sources*, 2018, **400**, 198–203.
44 S. N. S. Hapuarachchi, Z. Sun and C. Yan, *Adv. Sustainable Syst.*, 2018, **2**, 1–29.
45 S. Krachkovskiy, M. L. Trudeau and K. Zaghib, *Materials*, 2020, **13**, 1694.
46 H. Wang, E. Rus, T. Sakuraba, J. Kikuchi, Y. Kiya and H. D. Abruna, *Anal. Chem.*, 2014, **86**, 6197–6201.
47 B. B. Berkes, A. Jozwiuk, M. Vračar, H. Sommer, T. Brezesinski and J. Janek, *Anal. Chem.*, 2015, **87**, 5878–5883.
48 H. M. Hollmark, K. Maher, I. Saadoune, T. Gustafsson, K. Edström and L. C. Duda, *Phys. Chem. Chem. Phys.*, 2011, **13**, 6544–6551.
49 L. C. Duda and K. Edström, *J. Electron Spectrosc. Relat. Phenom.*, 2017, **221**, 79–87.
50 G. Wei, L. Wei, D. Wang, Y. Chen, Y. Tian, S. Yan, L. Mei and J. Jiao, *Sci. Rep.*, 2017, **7**, 1–8.
51 C. B. Frick and K. Edstroem, *Acta Cryst*, 2016, 281–282.
52 K. Yamamoto, Y. Iriyama and T. Hirayama, *Microsc.*, 2017, **66**, 50–61.
53 W. Du, Z. Hao, F. Iacoviello, L. Sheng, S. Guan, Z. Zhang, D. J. L. Brett, F. R. Wang and P. R. Shearing, *Small Methods*, 2021, **5**, 1–13.
54 K. Mizushima, P. C. Jones, P. J. Wiseman and J. B. Goodenough, *Solid State Ionics*, 1981, **3–4**, 171–174.
55 P. G. M. G. S. R. Thomas, W. I. F. David and J. B. Goodenough, *Mater. Res. Bull.*, 1985, **21**, 162.
56 A. R. Armstrong and P. G. Bruce, *Nature*, 1996, **381**, 499–500.
57 N. Mohamed and N. K. Allam, *RSC Adv.*, 2020, **10**, 21662–21685.
58 Y. Yang, R. Xu, K. Zhang, S. J. Lee, L. Mu, P. Liu, C. K. Waters, S. Spence, Z. Xu, C. Wei, D. J. Kautz, Q. Yuan, Y. Dong, Y. S. Yu, X. Xiao, H. K. Lee, P. Pianetta, P. Cloetens, J. S. Lee, K. Zhao, F. Lin and Y. Liu, *Adv. Energy Mater.*, 2019, **9**(25), 1900674.
59 C. Tian, Y. Xu, W. H. Kan, D. Sokaras, D. Nordlund, H. Shen, K. Chen, Y. Liu and M. Doeff, *ACS Appl. Mater. Interfaces*, 2020, **12**, 11643–11656.
60 X. Wang, H. Zhou, Z. Chen and X. Meng, *Energy Storage Mater.*, 2022, **49**, 181–208.
61 H. H. Ryu, K. J. Park, D. R. Yoon, A. Aishova, C. S. Yoon and Y. K. Sun, *Adv. Energy Mater.*, 2019, **9**(44), 1902698.
62 J. M. Kim, X. Zhang, J. G. Zhang, A. Manthiram, Y. S. Meng and W. Xu, *Mater. Today*, 2021, **46**, 155–182.
63 B. Qiu, M. Zhang, L. Wu, J. Wang, Y. Xia, D. Qian, H. Liu, S. Hy, Y. Chen, K. An, Y. Zhu, Z. Liu and Y. S. Meng, *Nat. Commun.*, 2016, **7**, 1–10.
64 J. Liu, J. Wang, Y. Ni, K. Zhang, F. Cheng and J. Chen, *Mater. Today*, 2021, **43**, 132–165.
65 X. Feng, M. K. Song, W. C. Stolte, D. Gardenghi, D. Zhang, X. Sun, J. Zhu, E. J. Cairns and J. Guo, *Phys. Chem. Chem. Phys.*, 2014, **16**, 16931–16940.
66 F. Geng, B. B. Hu, C. Li, C. Zhao, O. Lafon, J. Trébosc, J. P. Amoureux, M. Shen and B. B. Hu, *J. Mater. Chem. A*, 2020, **8**, 16515–16526.
67 X. Cao, H. Li, Y. Qiao, M. Jia, P. He, J. Cabana and H. Zhou, *Energy Storage Mater.*, 2021, **38**, 1–8.
68 J. K. Papp, N. Li, L. A. Kaufman and A. J. Naylor, *Electrochim. Acta*, 2021, **368**, 137505.
69 H. J. Noh, S. Youn, C. S. Yoon and Y. K. Sun, *J. Power Sources*, 2013, **233**, 121–130.
70 Y. K. Sun, D. J. Lee, Y. J. Lee, Z. Chen and S. T. Myung, *ACS Appl. Mater. Interfaces*, 2013, **5**, 11434–11440.
71 H. Li, P. Zhou, F. Liu, H. Li, F. Cheng and J. Chen, *Chem. Sci.*, 2019, **10**, 1374–1379.
72 Z. Tang, D. Feng, Y. Xu, L. Chen, X. Zhang and Q. Ma, *Batteries*, 2023, **9**, 156.
73 P. Arora, R. E. White and M. Doyle, *J. Electrochem. Soc.*, 1998, **145**, 3647–3667.
74 Z. Lu and J. R. Dahn, *J. Electrochem. Soc.*, 2002, **149**, A815.
75 Y.-L. Heng, Z.-Y. Gu, J.-Z. Guo, X.-T. Yang, X.-X. Zhao and X.-L. Wu, *Energy Mater.*, 2022, **2**(3), 200017.
76 R. V. Chebiam, A. M. Kannan, F. Prado and A. Manthiram, *Electrochem. Commun.*, 2001, **3**, 624–627.
77 J. Chen, W. Deng, X. Gao, S. Yin, L. Yang, H. Liu, G. Zou, H. Hou and X. Ji, *ACS Nano*, 2021, **15**, 6061–6104.
78 H. Koga, L. Croguennec and M. Me, *J. Phys. Chem. C*, 2014, **118**, 5700–5709.
79 M. Saubanère, E. McCalla, J. M. Tarascon and M. L. Doublet, *Energy Environ. Sci.*, 2016, **9**, 984–991.
80 Y. Cai, L. Ku, L. Wang, Y. Ma, H. Zheng, W. Xu, J. Han, B. Qu, Y. Chen, Q. Xie and D. L. Peng, *Sci. China Mater.*, 2019, **62**, 1374–1384.
81 C. Julien, *Inorganics*, 2014, **2**, 132–154.
82 J. Wandt, A. T. S. Freiberg, A. Ogrodnik and H. A. Gasteiger, *Mater. Today*, 2018, **21**, 825–833.

83 E. Cho, K. Kim, C. Jung, S. W. Seo, K. Min, H. S. Lee, G. S. Park and J. Shin, *J. Phys. Chem. C*, 2017, **121**, 21118–21127.
84 J. Wang, B. Shen, Z. Wang, F. E. Alsaadi and K. H. Alharbi, *Int. J. Syst. Sci.*, 2021, **52**, 1675–1691.
85 R. Hausbrand, D. Becker and W. Jaegermann, *Prog. Solid State Chem.*, 2014, **42**, 175–183.
86 P. Zhang and S. H. Wei, *Electrochim. Acta*, 2018, **270**, 409–416.
87 S. He, H. Lin, L. Qin, Z. Mao, H. He, Y. Li and Q. Li, *J. Mater. Chem. A*, 2017, **5**, 2163–2171.
88 J. Xu, M. Sun, R. Qiao, S. E. Renfrew, L. Ma, T. Wu, S. Hwang, D. Nordlund, D. Su, K. Amine, J. Lu, B. D. McCloskey, W. Yang and W. Tong, *Nat. Commun.*, 2018, **9**, 1–10.
89 Y. Yu, P. Karayaylali, D. Sokaras, L. Giordano, R. Kou, C. Sun, F. Maglia, R. Jung, F. S. Gittleson and Y. Shao-horn, *Energy Environ. Sci*, 2021, **2**, 2322–2334.
90 G. Assat and J. M. Tarascon, *Nat. Energy*, 2018, **3**, 373–386.
91 X. Li, H. Guan, Z. Ma, M. Liang, D. Song, H. Zhang, X. Shi, C. Li, L. Jiao and L. Zhang, *J. Energy Chem.*, 2020, **48**, 195–202.
92 L. Qiu, M. Zhang, Y. Song, Y. Xiao, Z. Wu, W. Xiang, Y. Liu, G. Wang, Y. Sun, J. Zhang, B. Zhang and X. Guo, *EcoMat*, 2021, **3**, 1–23.
93 Y. Ma, Y. Zhou, C. Du, P. Zuo, X. Cheng, L. Han, D. Nordlund, Y. Gao, G. Yin, H. L. Xin, M. M. Doeff, F. Lin and G. Chen, *Chem. Mater.*, 2017, **29**, 2141–2149.
94 T. Minato and T. Abe, *Prog. Surf. Sci.*, 2017, **92**, 240–280.
95 W. Jiang, C. Yin, Y. Xia, B. Qiu, H. Guo, H. Cui, F. Hu and Z. Liu, *ACS Appl. Mater. Interfaces*, 2019, **11**, 14023–14034.
96 A. Bhandari, P. K. Gupta, J. Bhattacharya and R. G. S. Pala, *J. Electrochem. Soc.*, 2019, **166**, A2966–A2972.
97 Z. Bi, W. Huang, S. Mu, W. Sun, N. Zhao and X. Guo, *Nano Energy*, 2021, **90**, 106498.
98 J. Qiu, X. Liu, R. Chen, Q. Li, Y. Wang, P. Chen, L. Gan, S. J. Lee, D. Nordlund, Y. Liu, X. Yu, X. Bai, H. Li and L. Chen, *Adv. Funct. Mater.*, 2020, **30**, 1–8.
99 M. Yi, W. Li and A. Manthiram, *Chem. Mater.*, 2022, **34**, 629–642.
100 J. Feng, Z. Gao, L. Sheng, Z. Hao and F. R. Wang, *Carbon Energy*, 2021, **3**(3), 385–409.
101 M. He, L. Boulet-Roblin, P. Borel, C. Tessier, P. Novák, C. Villevieille and E. J. Berg, *J. Electrochem. Soc.*, 2016, **163**, A83–A89.
102 J. N. Zhang, Q. Li, Y. Wang, J. Zheng, X. Yu and H. Li, *Energy Storage Mater.*, 2018, **14**, 1–7.
103 K. Edström, T. Gustafsson and J. O. Thomas, *Electrochim. Acta*, 2004, **50**, 397–403.
104 D. Chen, M. A. Mahmoud, J. H. Wang, G. H. Waller, B. Zhao, C. Qu, M. A. El-Sayed and M. Liu, *Nano Lett.*, 2019, **19**, 2037–2043.
105 H. Wang, A. Tang and K. Wang, *Chin. J. Chem.*, 2011, **29**, 27–32.
106 X. Hou, K. Ohta, Y. Kimura, Y. Tamenori, K. Tsuruta, K. Amezawa and T. Nakamura, *Adv. Energy Mater.*, 2021, **11**, 1–10.
107 D. P. Finegan, M. Scheel, J. B. Robinson, B. Tjaden, I. Hunt, T. J. Mason, J. Millichamp, M. Di Michiel, G. J. Offer, G. Hinds, D. J. L. Brett and P. R. Shearing, *Nat. Commun.*, 2015, **6**(1), 6924.
108 D. Liu, J. Yang, J. Hou, J. Liao and M. Wu, *RSC Adv.*, 2021, **11**, 12771–12783.
109 A. Pokle, S. Ahmed, S. Schweidler, M. Bianchini, T. Brezesinski, A. Beyer, J. Janek and K. Volz, *ACS Appl. Mater. Interfaces*, 2020, **12**, 57047–57054.
110 S. Bak, E. Hu, Y. Zhou, X. Yu, S. D. Senanayake, S. Cho, K. Kim, K. Y. Chung, X. Yang and K. Nam, *Appl. Mater. Interfaces*, 2014, **6**, 22594–22601.
111 S. Bak, E. Hu, Y. Zhou, X. Yu, S. D. D. Senanayake, S. Cho, K. Kim, K. Y. Y. Chung, X. Yang and K. Nam, *Appl. Mater. Interfaces*, 2014, **6**, 22594–22601.
112 Z. Wang, Z. Wang, D. Xue, J. Zhao, X. Zhang, L. Geng, Y. Li, C. Du, J. Yao, X. Liu, Z. Rong, B. Guo, R. Fang, Y. Su, C. Delmas, S. J. Harris, M. Wagemaker, L. Zhang, Y. Tang, S. Zhang, L. Zhu and J. Huang, *Nano Energy*, 2023, **105**, 108016.
113 S. Bruckenstein and R. R. Gadde, *J. Am. Chem. Soc.*, 1971, **93**, 793–794.
114 O. Wolter and J. Heitbaum, *Ext. Abstr., Meet. - Int. Soc. Electrochem.*, 1984, **6**, 454–456.
115 P. Novák, J. C. Panitz, F. Joho, M. Lanz, R. Imhof and M. Coluccia, *J. Power Sources*, 2000, **90**, 52–58.
116 D. J. Xiong, L. D. Ellis, J. Li, H. Li, T. Hynes, J. P. Allen, J. Xia, D. S. Hall, I. G. Hill and J. R. Dahn, *J. Electrochem. Soc.*, 2017, **164**, A3025–A3037.
117 Z. Jusys, M. Binder, J. Schnaidt and R. J. Behm, *Electrochim. Acta*, 2019, **314**, 188–201.
118 R. Lundström and E. J. Berg, *J. Power Sources*, 2021, **485**, 229347.
119 A. R. Armstrong, M. Holzapfel, P. Novák, C. S. Johnson, S. H. Kang, M. M. Thackeray and P. G. Bruce, *J. Am. Chem. Soc.*, 2006, **128**, 8694–8698.
120 J. Zheng, S. Myeong, W. Cho, P. Yan, J. Xiao, C. Wang, J. Cho and J. G. Zhang, *Adv. Energy Mater.*, 2017, **7**(6), 1601284.
121 E. Hu, X. Yu, R. Lin, X. Bi, J. Lu, S. Bak, K. W. Nam, H. L. Xin, C. Jaye, D. A. Fischer, K. Amine and X. Q. Yang, *Nat. Energy*, 2018, **3**, 690–698.
122 N. Tsiouvaras, S. Meini, I. Buchberger and H. A. Gasteiger, *J. Electrochem. Soc.*, 2013, **160**, A471–A477.
123 A. J. Naylor, E. Makkos, J. Maibach, N. Guerrini, A. Sobkowiak, E. Björklund, J. G. Lozano, A. S. Menon, R. Younesi, M. R. Roberts, K. Edström, M. S. Islam and P. G. Bruce, *J. Mater. Chem. A*, 2019, **7**, 25355–25368.
124 J. Song, B. Li, Y. Chen, Y. Zuo, F. Ning, H. Shang, G. Feng, N. Liu, C. Shen, X. Ai and D. Xia, *Adv. Mater.*, 2020, **32**, 1–8.
125 Z. N. Taylor, A. J. Perez, J. A. Coca-Clemente, F. Braga, N. E. Drewett, M. J. Pitcher, W. J. Thomas, M. S. Dyer, C. Collins, M. Zanella, T. Johnson, S. Day, C. Tang, V. R. Dhanak, J. B. Claridge, L. J. Hardwick and M. J. Rosseinsky, *J. Am. Chem. Soc.*, 2019, **141**, 7333–7346.

126 E. Zhao, L. He, B. Wang, X. Li, J. Zhang, Y. Wu, J. Chen, S. Zhang, T. Liang, Y. Chen, X. Yu, H. Li, L. Chen, X. Huang, H. Chen and F. Wang, *Energy Storage Mater.*, 2019, **16**, 354–363.
127 D. Foix, M. Sathiya, E. McCalla, J. M. Tarascon and D. Gonbeau, *J. Phys. Chem. C*, 2016, **120**, 862–874.
128 R. Qiao, Q. Li, Z. Zhuo, S. Sallis, O. Fuchs, M. Blum, L. Weinhardt, C. Heske, J. Pepper, M. Jones, A. Brown, A. Spucces, K. Chow, B. Smith, P. A. Glans, Y. Chen, S. Yan, F. Pan, L. F. J. Piper, J. Denlinger, J. Guo, Z. Hussain, Y. De Chuang and W. Yang, *Rev. Sci. Instrum.*, 2017, **88**(3), DOI: 10.1063/1.4977592.
129 W. E. Gent, K. Lim, Y. Liang, Q. Li, T. Barnes, S. J. Ahn, K. H. Stone, M. McIntire, J. Hong, J. H. Song, Y. Li, A. Mehta, S. Ermon, T. Tyliszczak, D. Kilcoyne, D. Vine, J. H. Park, S. K. Doo, M. F. Toney, W. Yang, D. Prendergast and W. C. Chueh, *Nat. Commun.*, 2017, **8**, 2091.
130 R. A. House, J. J. Marie, M. A. Pérez-Osorio, G. J. Rees, E. Boivin and P. G. Bruce, *Nat. Energy*, 2021, **6**, 781–789.
131 R. A. House, G. J. Rees, M. A. Pérez-Osorio, J. J. Marie, E. Boivin, A. W. Robertson, A. Nag, M. Garcia-Fernandez, K. J. Zhou and P. G. Bruce, *Nat. Energy*, 2020, **5**, 777–785.
132 A. K. C. Estandarte, J. Diao, A. V. Llewellyn, A. Jnawali, T. M. M. Heenan, S. R. Daemi, J. J. Bailey, S. Cipiccia, D. Batey, X. Shi, C. Rau, D. J. L. Brett, R. Jervis, I. K. Robinson and P. R. Shearing, *ACS Nano*, 2021, **15**, 1321–1330.
133 L. Wang, A. Dai, W. Xu, S. Lee, W. Cha, R. Harder, T. Liu, Y. Ren, G. Yin, P. Zuo, J. Wang, J. Lu and J. Wang, *J. Am. Chem. Soc.*, 2020, **142**, 14966–14973.
134 A. Singer, M. Zhang, S. Hy, D. Cela, C. Fang, T. A. Wynn, B. Qiu, Y. Xia, Z. Liu, A. Ulvestad, N. Hua, J. Wingert, H. Liu, M. Sprung, A. V. Zozulya, E. Maxey, R. Harder, Y. S. Meng and O. G. Shpyrko, *Nat. Energy*, 2018, **3**, 641–647.
135 Y. S. Hong, X. Huang, C. Wei, J. Wang, J. N. Zhang, H. Yan, Y. S. Chu, P. Pianetta, R. Xiao, X. Yu, Y. Liu and H. Li, *Chem.*, 2020, **6**, 2759–2769.
136 J. Weng, D. Ouyang, Y. Liu, M. Chen, Y. Li, X. Huang and J. Wang, *J. Power Sources*, 2021, **509**, 230340.
137 W. Du, R. E. Owen, A. Jnawali, T. P. Neville, F. Iacoviello, Z. Zhang, S. Liatard, D. J. L. Brett and P. R. Shearing, *J. Power Sources*, 2022, **520**, 230818.
138 M. T. M. Pham, J. J. Darst, D. P. Finegan, J. B. Robinson, M. Thomas, M. Heenan, M. D. R. Kok, F. Iacoviello, R. Owen, W. Q. Walker, O. V. Magdysyuk, T. Connolley, E. Darcy, G. Hinds, D. J. L. Brett and R. Shearing, *J. Power Sources*, 2020, **470**, 228039.
139 S. M. Bak, Z. Shadike, R. Lin, X. Yu and X. Q. Yang, *NPG Asia Mater.*, 2018, **10**, 563–580.
140 N. M. Trease, I. D. Seymour, M. D. Radin, H. Liu, H. Liu, S. Hy, N. Chernova, P. Parikh, A. Devaraj, K. M. Wiaderek, P. J. Chupas, K. W. Chapman, M. S. Whittingham, Y. S. Meng, A. Van Der Van and C. P. Grey, *Chem. Mater.*, 2016, **28**, 8170–8180.
141 K. Märker, P. J. Reeves, C. Xu, K. J. Griffith and C. P. Grey, *Chem. Mater.*, 2019, **31**, 2545–2554.
142 C. P. Grey and N. Dupré, *Chem. Rev.*, 2004, **104**, 4493–4512.
143 A. Grenier, P. J. Reeves, H. Liu, I. D. Seymour, K. Märker, K. M. Wiaderek, P. J. Chupas, C. P. Grey and K. W. Chapman, *J. Am. Chem. Soc.*, 2020, **142**, 7001–7011.
144 C. Delmas, D. Carlier, G. Ceder, M. Ménétrier and C. P. Grey, *Phys. Rev. B: Condens. Matter Mater. Phys.*, 2003, **67**, 1–14.
145 E. N. Bassey, P. J. Reeves, I. D. Seymour and C. P. Grey, *J. Mater. Chem. A.*, 2022, **144**(41), 18714–18729.
146 X. Li, X. Li, L. Monluc, B. Chen, M. Tang, P. H. Chien, X. Feng, I. Hung, Z. Gan, A. Urban and Y. Y. Hu, *Adv. Energy Mater.*, 2022, **12**, 1–10.
147 L. A. O'Dell and R. W. Schurko, *Chem. Phys. Lett.*, 2008, **464**, 97–102.
148 H. Liu, C. Li, C. Zhao, W. Tong and B. Hu, *Energy Storage Mater.*, 2022, **50**, 55–62.
149 C. Zhao, C. Li, H. Liu, Q. Qiu, F. Geng, M. Shen, W. Tong, J. Li and B. Hu, *J. Am. Chem. Soc.*, 2021, **143**, 18652–18664.
150 M. Sathiya, J. B. Leriche, E. Salager, D. Gourier, J. M. Tarascon and H. Vezin, *Nat. Commun.*, 2015, **6**, 1–7.
151 B. Song, M. Tang, E. Hu, O. J. Borkiewicz, K. M. Wiaderek, Y. Zhang, N. D. Phillip, X. Liu, Z. Shadike, C. Li, L. Song, Y. Y. Hu, M. Chi, G. M. Veith, X. Q. Yang, J. Liu, J. Nanda, K. Page and A. Huq, *Chem. Mater.*, 2019, **31**, 3756–3765.
152 M. Tang, A. Dalzini, X. Li, X. Feng, P. Chien, L. Song and Y. Hu, DOI: 10.1021/acs.jpclett.7b01425.
153 M. V. Avdeev, I. A. Bobrikov and V. I. Petrenko, *Phys. Sci. Rev.*, 2019, **3**, 1–15.
154 J. J. Biendicho, M. Roberts, C. Offer, D. Noréus, E. Widenkvist, R. I. Smith, G. Svensson, K. Edström, S. T. Norberg, S. G. Eriksson and S. Hull, *J. Power Sources*, 2014, **248**, 900–904.
155 W. K. Pang, M. Alam, V. K. Peterson and N. Sharma, *J. Mater. Res.*, 2015, **30**, 373–380.
156 B. Vadlamani, K. An, M. Jagannathan and K. S. R. Chandran, *J. Electrochem. Soc.*, 2014, **161**, A1731–A1741.
157 N. Sharma and V. K. Peterson, *Electrochim. Acta*, 2013, **101**, 79–85.
158 A. Senyshyn, M. J. Mühlbauer, K. Nikolowski, T. Pirling and H. Ehrenberg, *J. Power Sources*, 2012, **203**, 126–129.
159 M. M. Thackeray, *J. Electrochem. Soc.*, 1995, **142**, 2558–2563.
160 I. A. Bobrikov, A. M. Balagurov, C. W. Hu, C. H. Lee, T. Y. Chen, S. Deleg and D. A. Balagurov, *J. Power Sources*, 2014, **258**, 356–364.
161 A. S. Andersson and J. O. Thomas, *J. Power Sources*, 2001, **97**, 498–502.
162 N. Sharma, D. H. Yu, Y. Zhu, Y. Wu and V. K. Peterson, *J. Power Sources*, 2017, **342**, 562–569.
163 M. A. Rodriguez, M. H. Van Benthem, D. Ingersoll, S. C. Vogel and H. M. Reiche, *Powder Diffr.*, 2010, **25**, 143–148.
164 X. L. Wang, K. An, L. Cai, Z. Feng, S. E. Nagler, C. Daniel, K. J. Rhodes, A. D. Stoica, H. D. Skorpenske, C. Liang, W. Zhang, J. Kim, Y. Qi and S. J. Harris, *Sci. Rep.*, 2012, **2**, 1–7.
165 O. Dolotko, A. Senyshyn, M. J. Mühlbauer, K. Nikolowski and H. Ehrenberg, *J. Power Sources*, 2014, **255**, 197–203.

166 N. Paul, J. Keil, F. M. Kindermann, S. Schebesta, O. Dolotko, M. J. Mühlbauer, L. Kraft, S. V. Erhard, A. Jossen and R. Gilles, *J. Energy Storage*, 2018, **17**, 383–394.
167 J. Zhao, W. Zhang, A. Huq, S. T. Misture, B. Zhang, S. Guo, L. Wu, Y. Zhu, Z. Chen, K. Amine, F. Pan, J. Bai and F. Wang, *Adv. Energy Mater.*, 2017, **7**, 1–13.
168 E. Zhao, M. Zhang, X. Wang, E. Hu, J. Liu, X. Yu, M. Olguin, T. A. Wynn, Y. S. Meng, K. Page, F. Wang, H. Li, X. Q. Yang, X. Huang and L. Chen, *Energy Storage Mater.*, 2020, **24**, 384–393.
169 H. Liu, Y. Chen, S. Hy, K. An, S. Venkatachalam, D. Qian, M. Zhang and Y. S. Meng, *Adv. Energy Mater.*, 2016, **6**, 1–7.
170 P. E. Pearce, A. J. Perez, G. Rousse, M. Saubanère, D. Batuk, D. Foix, E. Mccalla, A. M. Abakumov, G. Van Tendeloo, M. Doublet and J. Tarascon, *Nat. Mater.*, 2017, **16**, 580–586.
171 E. Zhao, Q. Li, F. Meng, J. Liu, J. Wang, L. He, Z. Jiang, Q. Zhang, X. Yu, L. Gu, W. Yang, H. Li, F. Wang and X. Huang, *Angew. Chem., Int. Ed.*, 2019, **58**, 4323–4327.
172 A. J. Louli, A. Eldesoky, R. Weber, M. Genovese, M. Coon, Z. Deng, R. T. White, J. Lee, T. Rodgers, R. Petibon, S. Hy, S. J. H. Cheng and J. R. Dahn, DOI: **10.1038/s41560-020-0668-8**.
173 Z. Deng, X. Lin, Z. Huang, J. Meng, Y. Zhong, G. Ma, Y. Zhou, Y. Shen, H. Ding and Y. Huang, *Adv. Energy Mater.*, 2021, **11**, 1–24.
174 Z. Deng, Z. Huang, Y. Shen, Y. Huang, H. Ding, A. Luscombe, M. Johnson, J. E. Harlow, R. Gauthier and J. R. Dahn, *Joule*, 2020, **4**, 2017–2029.
175 S. Rosy, S. Haber, E. Evenstein, A. Saha, O. Brontvein, Y. Kratish, D. Bravo-Zhivotovskii, Y. Apeloig, M. Leskes and M. Noked, *Energy Storage Mater.*, 2020, **33**, 268–275.
176 C. Huang, Z. Wang, H. Wang, D. Huang, Y. bing He and S. X. Zhao, *Mater. Today Energy*, 2022, **29**, 101116.
177 A. Manthiram, J. C. Knight, S. T. Myung, S. M. Oh and Y. K. Sun, *Adv. Energy Mater.*, 2016, **6**(1), 1501010.
178 L. Liang, W. Zhang, F. Zhao, D. K. Denis, F. uz Zaman, L. Hou and C. Yuan, *Adv. Mater. Interfaces*, 2020, **7**, 1–34.
179 J. Hong, H. D. Lim, M. Lee, S. W. Kim, H. Kim, S. T. Oh, G. C. Chung and K. Kang, *Chem. Mater.*, 2012, **24**, 2692–2697.
180 L. Wang, T. Liu, A. Dai, V. De Andrade, Y. Ren, W. Xu, S. Lee, Q. Zhang, L. Gu, S. Wang, T. Wu, H. Jin and J. Lu, *Nat. Commun.*, 2021, **12**, 5370.